Dimensional reduction of a poromechanical cardiac model for myocardial perfusion studies

Radomír Chabiniok, Bruno Burtschell, Dominique Chapelle, Philippe Moireau

Applications in Engineering Science 12 (2022) 100121

Contents lists available at ScienceDirect

Applications in Engineering Science

journal homepage: www.elsevier.com/locate/apples

Dimensional reduction of a poromechanical cardiac model for myocardial perfusion studies

Radomír Chabiniok [a,b,*], Bruno Burtschell [a], Dominique Chapelle [a], Philippe Moireau [a]

[a] Inria & Ecole Polytechnique, CNRS, Institut Polytechnique de Paris, 1 rue Honoré d'Estienne d'Orves, 91128, Palaiseau, France
[b] Division of Pediatric Cardiology, Department of Pediatrics, UT Southwestern Medical Center, 5323 Harry Hines Blvd, 75390, Dallas, TX, USA

ARTICLE INFO

Keywords:
Poroelasticity
Biomechanical modeling
Computational physiology
Myocardial perfusion
Ischemic heart disease
Microvascular disease

ABSTRACT

In this paper, we adapt a previously developed poromechanical formulation to model the perfusion of myocardium during a cardiac cycle. First, a complete model is derived in 3D. Then, we perform a dimensional reduction under the assumption of spherical symmetry and propose a numerical algorithm that enables us to perform simulations of the myocardial perfusion throughout the cardiac cycle. These simulations illustrate the use of the proposed model to represent various physiological and pathological scenarios, specifically the vasodilation in the coronary network (to reproduce the standard clinical assessment of myocardial perfusion and perfusion reserve), the stenosis of a large coronary artery, an increased vascular resistance in the microcirculation (microvascular disease) and the consequences of inotropic activation (increased myocardial contractility) particularly at the level of the systolic flow impediment. Our results show that the model gives promising qualitative reproductions of complex physiological phenomena. This paves the way for future quantitative studies using clinical or experimental data.

1. Introduction

The heart muscle – called myocardium – is supplied with the coronary artery flow representing ~5% of the left ventricular output. The coronary artery flow is considerably reduced during heart contraction (systole), as stresses squeeze the sub-endocardial vessels. This phenomenon is called the systolic flow impediment (Westerhof et al., 2006; Kajiya et al., 2007).

The myocardial perfusion stands for the passage of blood through the myocardium via the network of coronary vessels. It allows bringing oxygen and removing carbon dioxide and metabolic waste products produced by the cells. It is typically quantified as a perfusion flow rate per 100 gram of myocardial tissue (physiologically ~1 mL/sec/100 g). Most tissues in the body remove at rest approximately 40% of the oxygen contained in arterial blood, leaving a sufficient reserve to cover an increased demand such as at the onset of exercise (Hall and Hall, 2020). In this respect, the coronary arteries are exceptional, as the myocardium removes ~80% of the arterial oxygen at rest. The reserve of blood oxygen content in myocardium is therefore limited and any increased demand of the cardiac muscle cells (cardiomyocytes) must be immediately compensated by an increase of myocardial perfusion.

The increased perfusion is a consequence of rapid dilation of the coronary arteries and of the increased cardiac output. The former is mostly a response of coronary arterioles to the vasodilation substances released by the cardiomyocytes lacking oxygen (such as adenosine, with one of the strongest vasodilation effects) — the process called coronary autoregulation. Secondly, an increased cardiac output during exercise – mostly given by chronotropic (increased heart rate) and inotropic (increased myocardial contractility) effects – also contributes to the increased coronary artery flow.

In the healthy myocardium, the level of perfusion under stress (e.g. during exercise) can increase three- to fourfold compared with the perfusion flow at rest — which factor represents the so-called myocardial perfusion reserve. The perfusion reserve is particularly important when considering earlier stages of coronary vasculature pathology, in which the level of myocardial perfusion at rest may be compensated, at the cost of a lower reserve to cover the demands at stress, however. The clinical assessment of myocardial perfusion is therefore typically performed under the maximum coronary vasodilation – e.g. by administering adenosine – to evaluate the perfusion reserve.

Myocardial perfusion is affected in patients with ischemic heart disease (IHD), in which there is an insufficient blood supply in a part of the myocardium. IHD represents one of the main causes of heart failure (HF). The myocardial perfusion (and perfusion reserve) is often affected already at earlier stages of HF, in which the therapeutic

* Corresponding author at: Division of Pediatric Cardiology, Department of Pediatrics, UT Southwestern Medical Center, 5323 Harry Hines Blvd, 75390, Dallas, TX, USA.
E-mail address: Radomir.Chabiniok@UTSouthwestern.edu (R. Chabiniok).

https://doi.org/10.1016/j.apples.2022.100121
Received 14 September 2022; Received in revised form 10 November 2022; Accepted 10 November 2022
Available online 14 November 2022

action could be the most efficient. However, a detailed assessment of such complex phenomena in individual patients is a great challenge. For example, an increased heart contractility (inotropic activation) increases the cardiac output. However, the increased active stresses in the myocardium could substantially reinforce the flow impediment. The insufficient myocardial perfusion would then limit the maximum achievable contractility and could induce symptoms of HF (e.g. dyspnea due to blood congestion in the lungs, or angina pain due to the accumulation of waste products within the myocardium). Likewise, a higher heart rate may lead to an increased cardiac output. However, the reduced period of heart relaxation (diastole), during which the major part of coronary artery flow occurs, may affect the myocardial perfusion and subsequently the performance of the heart, and could also possibly lead to HF symptoms. Understanding the interaction between the coronary circulation and cardiac mechanics is therefore of utmost interest for patients with IHD. Furthermore, distinguishing the role of narrowed large coronary arteries vs. pathological remodeling in the microcirculation in a given patient can have direct consequences on the optimal clinical management. In this respect, the efficiency of angioplasty with a stent placement or surgical coronary artery bypass grafting could be limited if the predominant cause lies in the microcirculation.

There has been a substantial development of non-invasive methods, e.g. perfusion magnetic resonance imaging (MRI) (Plein et al., 2007; Sammut et al., 2018). Nowadays, signal processing methods based on the signal deconvolution approach (Jerosch-Herold et al., 1998) are used for a quantitative evaluation of clinical perfusion MRI. However, the phenomenological model in use does not incorporate physiological modulations (e.g. inotropic and chronotropic effect), which are important in the objective assessment of a given patient. Moreover, these methods do not allow to directly distinguish between the component of flow in large and small vessel compartments, which is yet another limitation.

Biomechanical models of the heart contraction combined with the myocardial perfusion, e.g. visco-elastic model of myocardium with an active contractile component combined with a porous media flow modeling the flow in the coronary vascular network (see e.g. (Chabiniok et al., 2016; Lee et al., 2015) and references therein) have the potential to address some of these clinical questions. A general poromechanical formulation has been proposed by Chapelle and Moireau (2014) to address the specific modeling difficulties featured by cardiac perfusion, namely, large strains and rapid flows.

Poromechanical formulations represent a special case of a general approach to mixtures. A formal mathematical basis for interacting continua was given by Truesdell in a series of works, see e.g. (Truesdell, 1962). The review articles, such as (Atkin and Craine, 1976a; Bowen, 1976; Atkin and Craine, 1976b), book by Rajagopal and Tao (1995) or a more recent article by Klika (2014) provide numerous references to the use of the theory. The pioneering works were further refined using general descriptions of continuum mechanics to express the fundamental principles of conservation laws and thermodynamics e.g. in (Bowen, 1980; Coussy, 2004; Loret and Simões, 2005).

The computational intensity of such poromechanical models would, however, limit the possibility of implementing such models in clinical environments. The dimensional reduction of a cardiac model performed in (Caruel et al., 2014), in which the geometry and kinematics of a cardiac ventricle are assumed to have spherical symmetry while keeping the material properties as in the 3D model of Chapelle et al. (2012), has proven to be very cost-effective in the calculation and allowed to reproduce realistic cardiac cycles outputs in clinical proof-of-concept studies (Ruijsink et al., 2020; Le Gall et al., 2020; Gusseva et al., 2021). Therefore, in the present work we aim to explore the relevance of integrating the coronary circulation in this reduced-order model. We hypothesize that, while much easier to use, the fast running model will allow reproducing phenomena of physiological and clinical interest.

Specifically, in this article we propose to adapt the poromechanical formulation developed in (Chapelle and Moireau, 2014) to model the perfusion of myocardium by the coronaries. First, a complete model is derived in 3D. Then, we perform a dimensional reduction and propose a numerical algorithm that enables us to perform simulations of the myocardial perfusion throughout the cardiac cycle. These simulations illustrate the use of the proposed model to represent various physiological and pathological scenarios, specifically the vasodilation in the coronary network (to reproduce the standard clinical assessment of perfusion), the stenosis of a large coronary artery, an increased vascular resistance in the microcirculation (microvascular disease) and the consequences of inotropic activation particularly at the level of the systolic flow impediment.

2. A 3D cardiac model with perfused myocardium

The multi-scale cardiac model proposed by Sainte-Marie et al. (2006) and Chapelle et al. (2012) uses a hyperelastic potential for the description of the myocardium passive behavior. In this section, we propose to extend this formulation by adapting the poromechanical formulation introduced by Chapelle and Moireau (2014) and compatible with large deformations, in order to take into account the blood perfusion provided by the coronary network.

2.1. Poromechanical formulation

We start with the strong form of the poromechanical model proposed by Chapelle and Moireau (2014). Considering the following deformation map between the reference configuration Ω^0 and the deformed configuration Ω_t

$$\underline{\varphi} : \begin{cases} \Omega^0 \times \mathbb{R}^+ & \to \Omega_t \\ (\underline{\xi}, t) & \mapsto \underline{x} \end{cases}$$

we denote by $(\underline{y}_s, \underline{v}_s, \underline{v}_f, m)$ the system variable corresponding to the solid displacement and velocity, the fluid velocity and the added fluid mass such that the $\rho_0 + m = \rho_s(1-\phi) + \rho_f\phi$ where ρ_0, ρ_s and ρ_f are the mixture, solid and fluid reference density and ϕ is the porosity, namely, the fluid volume fraction. The system equations read (Chapelle and Moireau, 2014)

$$\begin{cases} \rho_s(1-\phi)\partial_t \underline{v}_s + \rho_f \phi \partial_t \underline{v}_f - \underline{\nabla}_{\underline{\xi}} \cdot (\underline{\underline{F}} \cdot \underline{\underline{\Sigma}}) = 0, & \text{in } \Omega^0, \quad \text{(a)} \\ \frac{1}{J}\partial_t (J \rho_f \phi \underline{v}_f) + \underline{\nabla}_{\underline{x}} \cdot (\rho_f \phi \underline{v}_f \otimes (\underline{v}_f - \underline{v}_s)) - \theta \underline{v}_f \\ \quad + \phi \underline{\underline{k}}_f^{-1} \cdot (\underline{v}_f - \underline{v}_s) + \underline{\nabla}_{\underline{x}} p - \frac{1}{\phi} \underline{\nabla}_{\underline{x}} \cdot (\phi \underline{\underline{\sigma}}_{vis}) = 0, & \text{in } \Omega_t, \quad \text{(b)} \\ \frac{1}{J}\frac{dm}{dt} + \underline{\nabla}_{\underline{x}} \cdot (\rho_f \phi (\underline{v}_f - \underline{v}_s)) = \theta, & \text{in } \Omega_t \quad \text{(c)} \end{cases} \tag{1}$$

where $\underline{\underline{F}}$ is the deformation gradient tensor with $J = \det(\underline{\underline{F}})$, $\underline{\underline{\Sigma}}$ the second Piola–Kirchhoff stress tensor, $\underline{\underline{k}}_f^{-1}$ the permeability tensor in deformed configuration, $\underline{\underline{\sigma}}_{vis}$ is the viscous part of the fluid Cauchy stress tensor and θ a volume source of fluid.

In the sequel we will use equivalent variational forms of (1)(a)–(1)(b), summarized as (Chapelle and Moireau, 2014)

$$\begin{cases} \mathcal{P}_a^s(\underline{v}^*) + \mathcal{P}_a^f(\underline{v}^*) + \mathcal{P}_i(\underline{v}^*) = \mathcal{P}_e(\underline{v}^*), \quad \forall \underline{v}^* \in \mathcal{V} & \text{(a)} \\ \mathcal{P}_a^f(\underline{v}_f^*) + \mathcal{P}_i^f(\underline{v}_f^*) = \mathcal{P}_e^f(\underline{v}_f^*), \quad \forall \underline{v}_f^* \in \mathcal{V} & \text{(b)} \end{cases} \tag{2}$$

where:

- $\mathcal{P}_a^s(\underline{v}^*)$ and $\mathcal{P}_a^f(\underline{v}_f^*)$ denote the virtual powers of solid and fluid inertia forces associated with test velocity fields $\underline{v}^*$ and $\underline{v}_f^*$, respectively;
- $\mathcal{P}_i(\underline{v}^*)$ and $\mathcal{P}_i^f(\underline{v}_f^*)$ are the virtual powers of total stresses and fluid stresses, respectively;
- $\mathcal{P}_e(\underline{v}^*)$ and $\mathcal{P}_e^f(\underline{v}_f^*)$ are the virtual powers of external forces applied on the mixture and on the fluid, respectively;

see (Chapelle and Moireau, 2014) for detailed expressions.

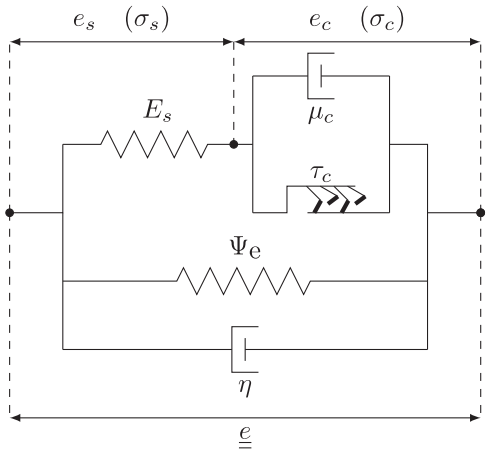

Fig. 1. Hill–Maxwell rheological model. Incorporation of the contractile unit into the solid constituent of the myocardium tissue.

2.2. An active constitutive law

In order to formulate an adequate constitutive law for the mixture, we combine the modeling ingredient of the active contraction introduced by Bestel et al. (2001), Sainte-Marie et al. (2006), Chapelle et al. (2012), Caruel et al. (2019), Kimmig et al. (2019) with the general poroelastic passive constitutive framework proposed by Chapelle and Moireau (2014).

The sarcomeres are the contractile units of muscle fibers at the micro-scale. Their shortening, and the resulting macroscopic contraction, is the consequence of the creation of *cross-bridges* (when myosin molecules of *thick filaments* periodically attach to surrounding thinner actin-made filaments) in the presence of calcium and adenosine triphosphate (ATP). Previous works on muscles modeling (Chapelle et al., 2012) have described the active stiffness k_c and the tension generated in the tissue per unit area of fiber cross-section (in the reference configuration) τ_c by the dynamical system

$$\begin{cases} \dot{k}_c = -(|u| + \alpha|\dot{e}_c|)k_c + n_0 k_0 |u|_+ \\ \dot{\tau}_c = -(|u| + \alpha|\dot{e}_c|)\tau_c + n_0\sigma_0|u|_+ + k_c\dot{e}_c, \end{cases}$$

where u denotes a variable reaction rate summarizing chemical activation ($|u|_+$ its positive values), e_c is the sarcomere extension, σ_0 is the maximum active stress, $\alpha|\dot{e}_c|$ accounts for bridges destruction upon rapid length changes, $n_0(e_c)$ is a length dependence function accounting for the Frank–Starling mechanism, and k_0 a stiffness parameter within the sarcomere. Note that this model of reduced complexity has been justified as a reduction of more complex stochastic models or Huxley based models (Caruel et al., 2019) or by experimental comparison (Caruel et al., 2014).

To incorporate the above contractile modeling into the overall behavior of the solid constituent of the myocardium tissue, we use a Hill–Maxwell rheological model (for strains e and stresses σ) recently proposed by Kimmig et al. (2019), see Fig. 1. The contractile element is placed in parallel with a linear damping element of viscous parameter μ_c, so that the tension in a fiber reads

$$\tau_{\text{fib}} = \tau_c + \mu_c\dot{e}_c.$$

This association is placed in series with a linear elastic element of Young's modulus E_s, satisfying $\sigma_s = E_s e_s$. This whole branch is assumed to produce stresses $\sigma_{1D}\,\underline{\tau}_1 \otimes \underline{\tau}_1$ along the fiber direction – where $\underline{\tau}_1$ is a unit vector associated with the fiber direction – and $\lambda\sigma_{1D}$ along directions transverse to $\underline{\tau}_1$, and is placed in parallel with the passive behavior of the myocardium solid tissue (a viscous branch and a hyperelastic potential).

Then, we adopt the non-linear rheology model proposed by Kimmig et al. (2019); strains and stresses of the first branch satisfy the following relations (extensions of the usual series-type rheological identities)

$$\begin{cases} \sigma_{1D} = \dfrac{\tau_{\text{fib}}}{1 + e_{\text{fib}}} \\ \tau_{\text{fib}} = \tau_c + \mu_c\dot{e}_c = E_s e_s = E_s(e_{\text{fib}} - e_c), \end{cases}$$

where the total (local) extension of a fiber $e_{\text{fib}} = e_s + e_c$ can be directly computed from the 3D Green–Lagrange strain tensor by use of

$$1 + e_{\text{fib}} = \sqrt{1 + 2\underline{\tau}_1 \cdot \underline{\underline{e}} \cdot \underline{\tau}_1}.$$

We assume here that the active stress σ_{1D} along $\underline{\tau}_1$ also produces stresses along directions transverse to the fiber, with a factor λ. Then, according to Chapelle and Moireau (2014), and integrating the active contribution, we consider a total second Piola–Kirchhoff stress tensor for the mixture of the following form

$$\underline{\underline{\Sigma}} = \phi\underline{\underline{\Sigma}}_{\text{vis}} + \frac{\partial\Psi(\underline{\underline{e}}, m)}{\partial\underline{\underline{e}}}\Big|_m + \frac{\partial\Psi^{\text{damp}}(\underline{\underline{e}}, \dot{\underline{\underline{e}}})}{\partial\dot{\underline{\underline{e}}}} + \lambda\sigma_{1D}\underline{\underline{\mathbb{1}}} + (1-\lambda)\sigma_{1D}\underline{\tau}_1 \otimes \underline{\tau}_1,$$

with $\Psi(\underline{\underline{e}}, m)$ the Helmholtz free energy of the mixture, and $\Psi^{\text{damp}} = \frac{\eta}{2}\,\text{tr}(\dot{\underline{\underline{e}}})^2$ a viscous pseudo-potential. Assumed to be incompressible, the fluid cannot store any energy, and therefore $\underline{\underline{\Sigma}}$ can be rewritten as (see (Chapelle and Moireau, 2014))

$$\underline{\underline{\Sigma}} = \phi\underline{\underline{\Sigma}}_{\text{vis}} + \frac{\partial\Psi_s(\underline{\underline{e}}, J_s)}{\partial\underline{\underline{e}}}\Big|_{J_s} - pJ\underline{\underline{C}}^{-1} + \frac{\partial\Psi^{\text{damp}}(\underline{\underline{e}}, \dot{\underline{\underline{e}}})}{\partial\dot{\underline{\underline{e}}}} + \lambda\sigma_{1D}\underline{\underline{\mathbb{1}}} + (1-\lambda)\sigma_{1D}\underline{\tau}_1 \otimes \underline{\tau}_1, \tag{3}$$

with $\Psi_s(\underline{\underline{e}}, J_s)$ being the solid energy where $J_s = J(1-\phi) = J - m/\rho_f - \phi_0$, and the pressure is given by

$$p = -\frac{\partial\Psi_s(\underline{\underline{e}}, J_s)}{\partial J_s}\Big|_{\underline{\underline{e}}} = \rho_f\frac{\partial\Psi(\underline{\underline{e}}, m)}{\partial m}\Big|_{\underline{\underline{e}}}. \tag{4}$$

We assume that the free energy functional can be constructed in the following manner

$$\Psi_s(\underline{\underline{e}}, J_s) = \Psi_e(\underline{\underline{e}}) + \Psi_{\text{bulk}}(J_s), \tag{5}$$

where Ψ_{bulk} describes how the energy depends on the solid phase volume changes, typically

$$\Psi_{\text{bulk}}(J_s) = \kappa_s\left[\frac{J_s}{1-\phi_0} - 1 - \log\left(\frac{J_s}{1-\phi_0}\right)\right], \tag{6}$$

and $\Psi_e(J_1, J_2, J_3, J_4)$ is a transverse-isotropic (with the fiber as privileged direction given by $\underline{\tau}_1$) hyperelastic potential representing the constitutive behavior of the skeleton, function of the classical reduced invariants of the right Cauchy–Green strain tensor

$$J_1 = I_1 I_3^{-1/3},\ J_2 = I_2 I_3^{-2/3},\ J_3 = I_3^{1/2},\ J_4 = I_4 I_3^{-1/3},$$

where the standard invariants I_i are defined by

$$I_1 = \text{tr}\,\underline{\underline{C}},\ I_2 = \frac{1}{2}\left((\text{tr}\,\underline{\underline{C}})^2 - \text{tr}(\underline{\underline{C}}^2)\right),\ I_3 = \det\underline{\underline{C}},\ I_4 = \underline{\tau}_1 \cdot \underline{\underline{C}} \cdot \underline{\tau}_1.$$

The hyperelastic part of the skeleton passive stress is derived by the chain rule

$$\frac{\partial\Psi_e}{\partial\underline{\underline{e}}} = 2\sum_i\left(\frac{\partial\Psi_e}{\partial J_i}\right)\left(\frac{\partial J_i}{\partial\underline{\underline{C}}}\right), \tag{7}$$

where the invariant derivatives are

$$\begin{cases} \dfrac{\partial J_1}{\partial \underline{\underline{C}}} = I_3^{-1/3}\left(\underline{\underline{I}} - \dfrac{1}{3} I_1 \underline{\underline{C}}^{-1}\right) \\ \dfrac{\partial J_2}{\partial \underline{\underline{C}}} = I_3^{-2/3}\left(I_1 \underline{\underline{I}} - \underline{\underline{C}} - \dfrac{2}{3} I_2 \underline{\underline{C}}^{-1}\right) \\ \dfrac{\partial J_3}{\partial \underline{\underline{C}}} = \dfrac{1}{2} I_3^{\frac{1}{2}}\, \underline{\underline{C}}^{-1} \\ \dfrac{\partial J_4}{\partial \underline{\underline{C}}} = I_3^{-1/3}\left(\underline{\tau}_1 \otimes \underline{\tau}_1 - \dfrac{1}{3} I_4 \underline{\underline{C}}^{-1}\right). \end{cases}$$

2.3. The cardiac system

The main external loading results from the intraventricular blood pressure P_v applied on the endocardium surface – denoted by Γ^0_{endo} in the reference configuration – and the associated traction force is given by $\underline{t}_0 = -P_v \underline{\underline{F}}^{-T} \cdot \underline{n}_e$, with $\underline{n}_e$ denoting the outward unit vector normal to Γ^0_{endo}. We then have

$$\mathcal{P}_e(\underline{v}^*_s) = -\int_{\Gamma^0_{\text{endo}}} P_v \underline{v}^*_s \cdot \underline{\underline{F}}^{-T} \cdot \underline{n}_e \, dS + \int_{\Gamma^0_{\text{epi}}} \underline{t}_0 \cdot \underline{v}^*_s \, dS,$$

where Γ^0_{epi} denotes the epicardial surface in the reference configuration.

According to Sainte-Marie et al. (2006), we model the opening and closure of the valves by the following relation that links P_v to the cardiac outflow $-\dot{V} = Q$ (with V the ventricular cavity volume),

$$-\dot{V} = Q = q(P_v, P_{ar}, P_{at}),$$

with P_{ar} and P_{at} the aorta (or pulmonary) and atrium pressures and q a regularized version of the ideal behavior

$$\begin{cases} Q \le 0 & \text{if } P_v = P_{at} \text{ (filling)}, \\ Q = 0 & \text{if } P_{at} \le P_v \le P_{ar} \text{ (isovolumic phases)}, \\ Q \ge 0 & \text{if } P_v = P_{ar} \text{ (ejection)}, \end{cases}$$

approximated by

$$\begin{cases} Q = K_{at}(P_v - P_{at}), & \text{if } P_v \le P_{at}, \\ Q = K_p(P_v - P_{at}), & \text{if } P_{at} \le P_v \le P_{ar}, \\ Q = K_{ar}(P_v - P_{ar}) + K_p(P_{ar} - P_{at}), & \text{if } P_v \ge P_{ar}, \end{cases}$$

where (K_{at}, K_p, K_{ar}) are constants satisfying $K_p \le \min(K_{at}, K_{ar})$.

In future works, the porous compartment will be coupled with 3D models of the largest coronary vessels, but for now it will be assumed to be only fed by a distributed source term θ according to (see also (Chapelle et al., 2009))

$$\theta = \rho_f k_{ca}(P_{ca} - p) - \rho_f k_{cv}(p - P_{cv}),$$

where k_{ca} (resp. k_{cv}) is constant and characterizes the small coronary arteries (resp. veins) conductance, P_{cv} the small veins pressure, and the coronary artery pressure P_{ca} is linked to the systemic circulation within the Windkessel model depicted in Fig. 2. The Windkessel model branches into two components, namely, the large coronary arteries (which further connect into the porous compartment of myocardium) and the remaining systemic circulation (with proximal and distal parts), represented by the system

$$\begin{cases} C_c \dot{P}_{ca} + \dfrac{P_{ca} - P_{ar}}{R_c} + \int_{\Omega_t} k_{ca}(P_{ca} - p)\, d\Omega = 0, & \text{(a)} \\ C_p \dot{P}_{ar} + \dfrac{P_{ar} - P_d}{R_p} + \dfrac{P_{ar} - P_{ca}}{R_c} = Q, & \text{(b)} \\ C_d \dot{P}_d + \dfrac{P_d - P_{ar}}{R_p} = \dfrac{P_{vs} - P_d}{R_d}, & \text{(c)} \end{cases} \tag{8}$$

with C_p, R_p, C_d, R_d and C_c, R_c being the capacitances and resistances of the proximal, distal and coronary circulations, P_d is the pressure in the distal systemic circulation, and P_{vs} represents the venous system pressure, see Fig. 2. Note that more complex circulation models

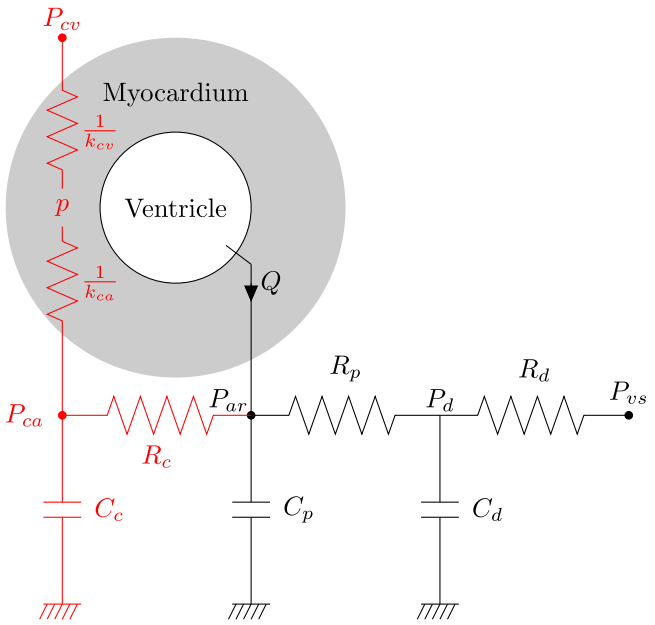

Fig. 2. Rheological model of the circulatory system plugged into the aorta. The branch in red models the coronaries. (For interpretation of the references to color in this figure legend, the reader is referred to the web version of this article.)

can also be considered as boundary conditions for the heart, see for instance (Manganotti et al., 2021).

All together, these elements give the following 3D cardiac system of equations

$$\begin{cases} \mathcal{P}^{\text{s}}_a(\underline{v}^*) + \mathcal{P}^{\text{f}}_a(\underline{v}^*) + \mathcal{P}_i(\underline{v}^*) = \mathcal{P}_e(\underline{v}^*) \quad \forall \underline{v}^* \in \mathcal{V} & \text{(a)} \\ \mathcal{P}^{\text{f}}_a(\underline{v}^*_{\text{f}}) + \mathcal{P}^{\text{f}}_i(\underline{v}^*_{\text{f}}) = \mathcal{P}^{\text{f}}_e(\underline{v}^*_{\text{f}}) \quad \forall \underline{v}^*_{\text{f}} \in \mathcal{V} & \text{(b)} \\ \frac{1}{J}\frac{\text{d}m}{\text{d}t} + \underline{\nabla}_{\underline{x}} \cdot (\rho_{\text{f}} \phi(\underline{v}_{\text{f}} - \underline{v}_{\text{s}})) = \rho_{\text{f}} k_{ca}(P_{ca} - p) - \rho_{\text{f}} k_{cv}(p - P_{cv}) & \text{(c)} \\ p = -\frac{\partial \Psi_{\text{bulk}}}{\partial J_{\text{s}}} & \text{(d)} \\ \underline{\underline{\Sigma}} = \phi \underline{\underline{\Sigma}}_{\text{vis}} + \frac{\partial \Psi_{\text{e}}}{\partial \underline{\underline{e}}} + \frac{\partial \Psi^{\text{damp}}}{\partial \dot{\underline{\underline{e}}}} - pJ\underline{\underline{C}}^{-1} + \lambda \sigma_{1\text{D}} \underline{\underline{\mathbb{1}}} + (1-\lambda)\sigma_{1\text{D}} \underline{\tau}_1 \otimes \underline{\tau}_1 & \text{(e)} \\ \sigma_{1\text{D}} = \tau_{\text{fib}}/(1 + e_{\text{fib}}) & \text{(f)} \\ e_{\text{fib}} = \sqrt{1 + 2\underline{\tau}_1 \cdot \underline{\underline{e}} \cdot \underline{\tau}_1} - 1 & \text{(g)} \\ \tau_{\text{fib}} = \tau_c + \mu_c \dot{e}_c = E_s(e_{\text{fib}} - e_c) & \text{(h)} \\ \dot{k}_c = -(|u| + \alpha|\dot{e}_c|)k_c + n_0 k_0 |u|_+ & \text{(i)} \\ \dot{\tau}_c = -(|u| + \alpha|\dot{e}_c|)\tau_c + n_0 \sigma_0 |u|_+ + k_c \dot{e}_c & \text{(j)} \\ -\dot{V} = Q = q(P_v, P_{ar}, P_{at}) & \text{(k)} \\ C_c \dot{P}_{ca} + (P_{ca} - P_{ar})/R_c + \int_{\Omega_t} k_{ca}(P_{ca} - p)\, d\Omega = 0 & \text{(l)} \\ C_p \dot{P}_{ar} + (P_{ar} - P_d)/R_p + (P_{ar} - P_{ca})/R_c = Q & \text{(m)} \\ C_d \dot{P}_d + (P_d - P_{ar})/R_p = (P_{vs} - P_d)/R_d. & \text{(n)} \end{cases} \tag{9}$$

3. Dimensional reduction of the cardiac model with poromechanics

3.1. 0D cardiac model

As proposed by Caruel et al. (2014) – see also (Manganotti et al., 2021) – we now perform a dimensional reduction of the above cardiac model. A ventricle is represented by a sphere of radius R_0 and thickness d_0 in the reference configuration Ω^0. We assume that this spherical symmetry is shared by the constitutive properties, and we apply an internal pressure P_v. As a consequence, for symmetry reasons, the deformed configuration is described by a sphere of radius R and thickness d. We define $(\underline{i}_r, \underline{i}_{\phi_1}, \underline{i}_{\phi_2})$ a local basis on Ω^0, with $\underline{i}_r$ radial, $\underline{i}_{\phi_1} = \underline{\tau}_1$ and $(\underline{i}_{\phi_1}, \underline{i}_{\phi_2})$ orthoradial, see Fig. 3. In our framework, the displacement

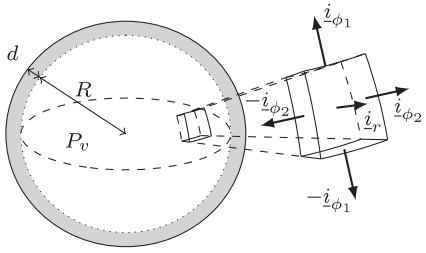

Fig. 3. Spherical model of a ventricle.

with respect to the reference configuration reads $\underline{y} = y\,\underline{i}_r = (R - R_0)\,\underline{i}_r$ and the right Cauchy–Green deformation tensor reduces to

$$\underline{\underline{C}} = \begin{pmatrix} C_{rr} & 0 & 0 \\ 0 & C & 0 \\ 0 & 0 & C \end{pmatrix}.$$

The circumferential lengths are scaled by $\sqrt{C} = 1 + y/R_0$ between the reference and deformed configurations. In passing, we note that, unlike in (Caruel et al., 2014), no incompressibility is assumed due to perfusion, in particular, and therefore $J = \det \underline{\underline{C}}^{1/2}$ has no reason to be 1. In addition, the relative thinness of the wall compared with the sphere radius combined with the equality $\underline{v}_\mathrm{f} = \underline{v}_\mathrm{s}$ on the endocardium surface justifies in this framework the assumption $\underline{v}_\mathrm{f} = \underline{v}_\mathrm{s}$ on the whole domain, and the introduction of the single notation $\underline{v}$ to denote both solid and fluid velocities. Therefore, (1)(b) is replaced by $\underline{v}_\mathrm{f} = \underline{v}_\mathrm{s}$, and multiplying (1)(a) by test functions $\underline{v}^*$ and integrating space-wise yields (assuming $\underline{f} = \underline{0}$)

$$\int_{\Omega^0} (\rho_0 + m) \frac{\mathrm{d}\underline{v}}{\mathrm{dt}} \cdot \underline{v}^*\, d\Omega + \int_{\Omega^0} \underline{\underline{\Sigma}} : d_{\underline{y}}\underline{\underline{e}} \cdot \underline{v}^*\, d\Omega = \int_{\Gamma^0_{\mathrm{endo}} \cup \Gamma^0_{\mathrm{epi}}} \underline{t}_0 \cdot \underline{v}^*\, dS. \quad (10)$$

Considering a radial virtual velocity $\underline{v}^* = v^* \underline{i}_r$ with the assumed kinematic symmetry, we find that

$$(d_{\underline{y}}\underline{\underline{e}} \cdot \underline{v}^*)_{\phi_1\phi_1} = (d_{\underline{y}}\underline{\underline{e}} \cdot \underline{v}^*)_{\phi_2\phi_2} = (1 + y/R_0)(v^*/R_0).$$

We neglect fluid viscous effects $\underline{\underline{\Sigma}}_{\mathrm{vis}}$. Thanks to the smallness of d/R, classical arguments of shell theory enable us to neglect the radial stress Σ_{rr} compared with the orthoradial components (Chapelle and Bathe, 2010), and to explicitly infer p from $\Sigma_{rr} = 0$ in (3), i.e.

$$p = \frac{C_{rr}}{J}\left[\left(\frac{\partial \Psi_\mathrm{e}}{\partial \underline{\underline{e}}}\right)_{rr} + \left(\frac{\partial \Psi^{\mathrm{damp}}}{\partial \dot{\underline{\underline{e}}}}\right)_{rr} + \lambda\sigma_{1\mathrm{D}}\right] = \frac{J}{C^2}\left[\left(\underline{\underline{\Sigma}}_p\right)_{rr} + \lambda\sigma_{1\mathrm{D}}\right], \quad (11)$$

where we define the 3D passive stress as

$$\underline{\underline{\Sigma}}_p = \frac{\partial \Psi_\mathrm{e}}{\partial \underline{\underline{e}}}(\underline{\underline{e}}) + \frac{\partial \Psi^{\mathrm{damp}}}{\partial \dot{\underline{\underline{e}}}}(\underline{\underline{e}}, \dot{\underline{\underline{e}}}). \quad (12)$$

Therefore, we have

$$\underline{\underline{\Sigma}} : \mathrm{d}_{\underline{y}}\underline{\underline{e}} \cdot \underline{v}^* = \left(1 + \frac{y}{R_0}\right)\frac{v^*}{R_0}\Sigma_{\mathrm{sph}},$$

with

$$\Sigma_{\mathrm{sph}} = \Sigma_{\phi_1\phi_1} + \Sigma_{\phi_2\phi_2} = \left(\underline{\underline{\Sigma}}_p\right)_{\phi_1\phi_1} + \left(\underline{\underline{\Sigma}}_p\right)_{\phi_2\phi_2} - 2J^2C^{-3}\left(\underline{\underline{\Sigma}}_p\right)_{rr} + \sigma_{1\mathrm{D}}(1 + \lambda - 2\lambda J^2 C^{-3}),$$

and J that can be obtained thanks to the following combination of (4), (5) and (11)

$$-\frac{\partial \Psi_{\mathrm{bulk}}}{\partial J_\mathrm{s}} = \frac{J}{C^2}\left[\left(\underline{\underline{\Sigma}}_p\right)_{rr} + \lambda\sigma_{1\mathrm{D}}\right].$$

Note that the passive stress $\underline{\underline{\Sigma}}_p$ is calculated with the chain rule (7), and that the invariants and their derivatives reduce to

$$\begin{cases} I_1 = C_{rr} + 2C = J^2C^{-2} + 2C \\ I_2 = C^2 + 2CC_{rr} = C^2 + 2J^2C^{-1} \\ I_3 = C_{rr}C^2 = J^2 \\ I_4 = C \end{cases}$$

and

$$\begin{cases} \dfrac{\partial J_1}{\partial \underline{\underline{C}}} = J^{-2/3}\left(\underline{\underline{\mathbb{1}}} - \dfrac{1}{3}(J^2C^{-2} + 2C)\underline{\underline{C}}^{-1}\right) \\ \dfrac{\partial J_2}{\partial \underline{\underline{C}}} = J^{-4/3}\left((J^2C^{-2} + 2C)\underline{\underline{\mathbb{1}}} - \underline{\underline{C}} - \dfrac{2}{3}(C^2 + 2J^2C^{-1})\underline{\underline{C}}^{-1}\right) \\ \dfrac{\partial J_3}{\partial \underline{\underline{C}}} = \dfrac{1}{2}J\underline{\underline{C}}^{-1} \\ \dfrac{\partial J_4}{\partial \underline{\underline{C}}} = J^{-2/3}\left(\underline{\tau}_1 \otimes \underline{\tau}_1 - \dfrac{1}{3}J^{-2/3}C\underline{\underline{C}}^{-1}\right) \end{cases}$$

while the viscosity within the skeleton gives

$$\frac{\partial \Psi^{\mathrm{damp}}}{\partial \dot{\underline{\underline{e}}}} = \frac{\eta}{2}\dot{\underline{\underline{C}}}.$$

With this, the derivation of Σ_{sph} gives

$$\Sigma_{\mathrm{sph}} = 4J^{-\frac{2}{3}}(1 - J^2C^{-3})\left(\frac{\partial \Psi_\mathrm{e}}{\partial J_1} + J^{-\frac{2}{3}}C\frac{\partial \Psi_\mathrm{e}}{\partial J_2}\right) + 2J^{-\frac{2}{3}}\frac{\partial \Psi_\mathrm{e}}{\partial J_4} + \sigma_{1\mathrm{D}}(1 + \lambda - 2\lambda J^2C^{-3}) + \eta\left(\dot{C} - 2J^3C^{-6}(\dot{J}C - J\dot{C})\right)$$

with $\sigma_{1\mathrm{D}}$ given by (9)(f).

Now, using that $d/d_0 = \sqrt{C_{rr}} = J(1 + \frac{y}{R_0})^{-2}$, the virtual work of pressure forces reads

$$\begin{aligned} \int_{\Gamma^0_{\mathrm{endo}}} \underline{t}_0 \cdot (v^*\underline{i}_r)\, dS &= 4\pi P_v\left(R - \frac{d}{2}\right)^2\left(1 + J\frac{d_0}{R_0}\left(1 + \frac{y}{R_0}\right)^{-3}\right)v^* \\ &= 4\pi P_v\left(R_0 + y - \sqrt{C_{rr}}\frac{d_0}{2}\right)^2\left(1 + J\frac{d_0}{R_0}\left(1 + \frac{y}{R_0}\right)^{-3}\right)v^* \\ &= 4\pi P_v R_0^2\left(1 + \frac{y}{R_0} - \frac{Jd_0}{2R_0}\left(1 + \frac{y}{R_0}\right)^{-2}\right)^2\left(1 + J\frac{d_0}{R_0}\left(1 + \frac{y}{R_0}\right)^{-3}\right)v^*, \end{aligned} \quad (13)$$

and we will neglect the traction forces at the epicardium (compared with pressure forces).

Integrating (10) over the sphere of radius R_0 and thickness d_0, we finally get the second-order ordinary differential equation (ODE) satisfied by the mixture displacement y,

$$\begin{cases} d_0(\rho_0 + m)\dfrac{\mathrm{d}^2y}{\mathrm{dt}^2} + \dfrac{d_0}{R_0}\left(1 + \dfrac{y}{R_0}\right)\Sigma_{\mathrm{sph}} \\ \quad = P_v\left(1 + \dfrac{y}{R_0} - \dfrac{Jd_0}{2R_0}\left(1 + \dfrac{y}{R_0}\right)^{-2}\right)^2\left(1 + J\dfrac{d_0}{R_0}\left(1 + \dfrac{y}{R_0}\right)^{-3}\right) \\ \dfrac{\mathrm{d}m}{\mathrm{dt}} = J\theta \end{cases} \quad (14)$$

where

$$\begin{cases} \Sigma_{\mathrm{sph}} = \left(\underline{\underline{\Sigma}}_p\right)_{\phi_1\phi_1} + \left(\underline{\underline{\Sigma}}_p\right)_{\phi_2\phi_2} - 2\dfrac{J^2}{C^3}\left(\underline{\underline{\Sigma}}_p\right)_{rr} \\ \quad +\sigma_{1\mathrm{D}}(1 + \lambda - 2\lambda J^2C^{-3}) \quad \text{(a)} \\ \text{and } J \text{ such that } -\dfrac{\partial \Psi_{\mathrm{bulk}}}{\partial J_\mathrm{s}} = \dfrac{J}{C^2}\left[\left(\underline{\underline{\Sigma}}_p\right)_{rr} + \lambda\sigma_{1\mathrm{D}}\right]. \quad \text{(b)} \end{cases} \quad (15)$$

Let us notice that unlike in (Caruel et al., 2014), y has to be completed by J, given by (15)(b), to fully characterize the 3D displacement field y. Our set of dynamic variables for the mixture mechanics is (y, v, m). Finally, the intraventricular volume reads in this context

$$V = \frac{4\pi}{3}\left(R - \frac{d}{2}\right)^3 = \frac{4\pi}{3}\left(R_0 + y - \sqrt{C_{rr}}\frac{d_0}{2}\right)^3 = \frac{4\pi}{3}\left(R_0 + y - \frac{J d_0}{2}\left(1 + \frac{y}{R_0}\right)^{-2}\right)^3,$$

so that its variations and the valve law (9)(k) become

$$\begin{aligned}\dot{V} &= 4\pi R_0^2\left(1 + \frac{y}{R_0} - \frac{J d_0}{2R_0}\left(1 + \frac{y}{R_0}\right)^{-2}\right)^2 \\ &\quad\times\left[\dot{y} - \frac{\dot{J} d_0}{2}\left(1 + \frac{y}{R_0}\right)^{-2} + \frac{J d_0}{R_0}\dot{y}\left(1 + \frac{y}{R_0}\right)^{-3}\right] \\ &= -f(P_v, P_{ar}, P_{at}).\end{aligned}$$

With these elements, the cardiac model with poromechanics (9) reduces to the following system on $(y, J, m, e_c, k_c, \tau_c, P_{ca}, P_{ar}, P_d)$

$$\begin{cases} d_0(\rho_0 + m)\frac{\mathrm{d}^2 y}{\mathrm{d}t^2} + \frac{d_0}{R_0}\left(1 + \frac{y}{R_0}\right)\Sigma_{\mathrm{sph}} \\ \quad = P_v\left(1 + \frac{y}{R_0} - \frac{J d_0}{2R_0}\left(1 + \frac{y}{R_0}\right)^{-2}\right)^2\left(1 + J\frac{d_0}{R_0}\left(1 + \frac{y}{R_0}\right)^{-3}\right) & \text{(a)} \\ \frac{1}{J}\frac{\mathrm{d}m}{\mathrm{d}t} = \theta = \rho_{\mathrm{f}} k_{ca}(P_{ca} - p) - \rho_{\mathrm{f}} k_{cv}(p - P_{cv}) & \text{(b)} \\ p = \frac{J}{C^2}\left[\left(\underline{\underline{\Sigma}}_p\right)_{rr} + \lambda\sigma_{1\mathrm{D}}\right] & \text{(c)} \\ -\frac{\partial\Psi_{\mathrm{bulk}}}{\partial J_{\mathrm{s}}} = \frac{J}{C^2}\left[\left(\underline{\underline{\Sigma}}_p\right)_{rr} + \lambda\sigma_{1\mathrm{D}}\right] & \text{(d)} \\ \Sigma_{\mathrm{sph}} = \left(\underline{\underline{\Sigma}}_p\right)_{\phi_1\phi_1} + \left(\underline{\underline{\Sigma}}_p\right)_{\phi_2\phi_2} - 2pJC^{-1} + \sigma_{1\mathrm{D}}(1 + \lambda) & \text{(e)} \\ \sigma_{1\mathrm{D}} = \tau_{\mathrm{fib}}/(1 + e_{\mathrm{fib}}) & \text{(f)} \\ \tau_{\mathrm{fib}} = \tau_c + \mu_c\dot{e}_c = E_s(e_{\mathrm{fib}} - e_c) & \text{(g)} \\ \dot{k}_c = -(|u| + \alpha|\dot{e}_c|)k_c + n_0 k_0|u|_+ & \text{(h)} \\ \dot{\tau}_c = -(|u| + \alpha|\dot{e}_c|)\tau_c + n_0\sigma_0|u|_+ + k_c\dot{e}_c & \text{(i)} \\ -\dot{V} = f(P_v, P_{ar}, P_{at}) & \text{(j)} \\ C_c\dot{P}_{ca} + (P_{ca} - P_{ar})/R_c + (P_{ca} - p)k_{ca}V_{myo} = 0 & \text{(k)} \\ C_p\dot{P}_{ar} + (P_{ar} - P_d)/R_p + (P_{ar} - P_{ca})/R_c = Q & \text{(l)} \\ C_d\dot{P}_d + (P_d - P_{ar})/R_p = (P_{vs} - P_d)/R_d & \text{(m)} \end{cases} \tag{16}$$

where V_{myo} denotes the total volume of myocardium in the reference configuration.

Remark 1. The following expressions of p and Σ_{sph} can be inferred from the derivatives of Ψ_{e}:

$$\begin{aligned} p &= \frac{4J^{1/3}}{3C^2}\left(1 - \frac{C^3}{J^2}\right)\left[\frac{\partial\Psi_{\mathrm{e}}}{\partial J_1} + \frac{C}{J^{2/3}}\frac{\partial\Psi_{\mathrm{e}}}{\partial J_2}\right] + \frac{\partial\Psi_{\mathrm{e}}}{\partial J_3} - \frac{2C}{3J^{7/3}}\frac{\partial\Psi_{\mathrm{e}}}{\partial J_4} \\ &\quad + \eta\frac{J^2}{C^5}(C\dot{J} - J\dot{C}) + \frac{J}{C^2}\lambda\sigma_{1\mathrm{D}} \\ \Sigma_{\mathrm{sph}} &= 4J^{-\frac{2}{3}}(1 - J^2C^{-3})\left(\frac{\partial\Psi_{\mathrm{e}}}{\partial J_1} + J^{-\frac{2}{3}}C\frac{\partial\Psi_{\mathrm{e}}}{\partial J_2}\right) + 2J^{-\frac{2}{3}}\frac{\partial\Psi_{\mathrm{e}}}{\partial J_4} \\ &\quad + \sigma_{1\mathrm{D}}\left(1 + \lambda - 2\lambda J^2C^{-3}\right) + \eta\left(\dot{C} - 2J^3C^{-6}(\dot{J}C - J\dot{C})\right) \end{aligned}$$

Remark 2 (*Solid Incompressibility*)**.** The limit $\kappa \to \infty$ in (4) and (6) gives the following relation for J, that replaces (16)(d) in the above system,

$$J = 1 + \frac{m}{\rho_{\mathrm{f}}}. \tag{17}$$

3.2. Energy balance at the continuous level in the reduced formulation

We recall that

$$\underline{\underline{e}} = \tfrac{1}{2}(\underline{\underline{C}} - \underline{\underline{\mathbb{1}}}) \text{ and } \underline{\underline{C}}(y, J) = \begin{pmatrix} \frac{J^2}{C(y)^2} & 0 & 0 \\ 0 & C(y) & 0 \\ 0 & 0 & C(y) \end{pmatrix},$$

with $C(y) = \dfrac{2y}{R_0} + \dfrac{y^2}{R_0^2} + 1$.

In order to establish an energy conservation at the continuous level, we remove the loadings $f = 0$ and $P_v = 0$, the active contribution $\sigma_{1\mathrm{D}} = 0$ and the solid damping $\eta = 0$. Our objective is to derive an energy balance in which we propose to keep a fluid source θ. Substituting (16)(e), the multiplication of (16)(a) by $v = \mathrm{d}y/\mathrm{d}t$ gives

$$\begin{aligned}&(\rho_0 + m)v\frac{\mathrm{d}v}{\mathrm{d}t} \\ &\quad + \left(1 + \frac{y}{R_0}\right)\frac{1}{R_0}\frac{\mathrm{d}y}{\mathrm{d}t}\left[\left(\frac{\partial\Psi_{\mathrm{e}}}{\partial\underline{\underline{e}}}\right)_{\phi_1\phi_1} + \left(\frac{\partial\Psi_{\mathrm{e}}}{\partial\underline{\underline{e}}}\right)_{\phi_2\phi_2} - 2pJC^{-1}\right] = 0.\end{aligned} \tag{18}$$

The first term gives

$$(\rho_0 + m)\frac{\mathrm{d}v}{\mathrm{d}t}v = \frac{\mathrm{d}}{\mathrm{d}t}\left(\frac{1}{2}(\rho_0 + m)v^2\right) - \frac{1}{2}\frac{\mathrm{d}m}{\mathrm{d}t}v^2 = \frac{\mathrm{d}E_c}{\mathrm{d}t} - \frac{1}{2}J\theta v^2,$$

with $E_c = \frac{1}{2}(\rho_0 + m)v^2$ the kinetic energy per unit volume of the mixture, and $\frac{1}{2}J\theta v^2$ its increment brought by the source term θ.

For the second term, we introduce $e = (\underline{\underline{e}})_{\phi_1\phi_1} = (\underline{\underline{e}})_{\phi_2\phi_2} = \frac{1}{2}(C - 1)$ that depends only on y in order to write

$$\left(1 + \frac{y}{R_0}\right)\frac{1}{R_0}\frac{\mathrm{d}y}{\mathrm{d}t} = \frac{\mathrm{d}}{\mathrm{d}t}\left(\frac{y}{R_0} + \frac{y^2}{2R_0^2}\right) = \frac{\mathrm{d}e}{\mathrm{d}t},$$

and the following expression for the derivative of the free energy

$$\begin{aligned}\frac{\mathrm{d}\Psi_{\mathrm{s}}}{\mathrm{d}t} &= \frac{\partial\Psi_{\mathrm{e}}}{\partial\underline{\underline{e}}}\frac{\mathrm{d}\underline{\underline{e}}}{\mathrm{d}t} + \frac{\partial\Psi_{\mathrm{bulk}}}{\partial J_{\mathrm{s}}}\left(\frac{\mathrm{d}J}{\mathrm{d}t} - \frac{1}{\rho_{\mathrm{f}}}\frac{\mathrm{d}m}{\mathrm{d}t}\right) \\ &= \left(\frac{\partial\Psi_{\mathrm{e}}}{\partial\underline{\underline{e}}}\right)_{rr}\frac{\mathrm{d}e_{rr}}{\mathrm{d}t} + \left(\frac{\partial\Psi_{\mathrm{e}}}{\partial\underline{\underline{e}}}\right)_{\phi_1\phi_1}\frac{\mathrm{d}e}{\mathrm{d}t} + \left(\frac{\partial\Psi_{\mathrm{e}}}{\partial\underline{\underline{e}}}\right)_{\phi_2\phi_2}\frac{\mathrm{d}e}{\mathrm{d}t} \\ &\quad + \frac{\partial\Psi_{\mathrm{bulk}}}{\partial J_{\mathrm{s}}}\left(\frac{\mathrm{d}J}{\mathrm{d}t} - \frac{1}{\rho_{\mathrm{f}}}\frac{\mathrm{d}m}{\mathrm{d}t}\right),\end{aligned}$$

where $e_{rr} = (\underline{\underline{e}})_{rr} = \frac{1}{2}\left(\frac{J^2}{C^2} - 1\right)$ and

$$\frac{\mathrm{d}e_{rr}}{\mathrm{d}t} = \frac{J}{C^2}\frac{\mathrm{d}J}{\mathrm{d}t} - \frac{J^2}{C^3}\frac{\mathrm{d}C}{\mathrm{d}t} = \frac{J}{C^2}\frac{\mathrm{d}J}{\mathrm{d}t} - 2\frac{J^2}{C^3}\frac{\mathrm{d}e}{\mathrm{d}t}.$$

With this, and using we write

$$\begin{aligned}\frac{\mathrm{d}\Psi_{\mathrm{s}}}{\mathrm{d}t} &= \left[\left(\frac{\partial\Psi_{\mathrm{e}}}{\partial\underline{\underline{e}}}\right)_{\phi_1\phi_1} + \left(\frac{\partial\Psi_{\mathrm{e}}}{\partial\underline{\underline{e}}}\right)_{\phi_2\phi_2} - 2pJC^{-1}\right]\frac{\mathrm{d}e}{\mathrm{d}t} + p\frac{\mathrm{d}J}{\mathrm{d}t} \\ &\quad + \frac{\partial\Psi_{\mathrm{bulk}}}{\partial J_{\mathrm{s}}}\left(\frac{\mathrm{d}J}{\mathrm{d}t} - \frac{1}{\rho_{\mathrm{f}}}\frac{\mathrm{d}m}{\mathrm{d}t}\right).\end{aligned}$$

We now use (16)(b) and (16)(d) to rewrite the above equation as

$$\frac{\mathrm{d}\Psi_{\mathrm{s}}}{\mathrm{d}t} = \left[\left(\frac{\partial\Psi_{\mathrm{e}}}{\partial\underline{\underline{e}}}\right)_{\phi_1\phi_1} + \left(\frac{\partial\Psi_{\mathrm{e}}}{\partial\underline{\underline{e}}}\right)_{\phi_2\phi_2} - 2pJC^{-1}\right]\frac{\mathrm{d}e}{\mathrm{d}t} + \frac{pJ\theta}{\rho_{\mathrm{f}}}.$$

Remark 3. In the incompressible solid limit the derivation of this expression relies on $\frac{\mathrm{d}J}{\mathrm{d}t} = \frac{1}{\rho_{\mathrm{f}}}\frac{\mathrm{d}m}{\mathrm{d}t} = \frac{J\theta}{\rho_{\mathrm{f}}}$.

Finally, (18) gives the following energy balance

$$\frac{\mathrm{d}(E_c + \Psi_{\mathrm{s}})}{\mathrm{d}t} = J\theta\left(\frac{1}{2}v^2 + \frac{p}{\rho_{\mathrm{f}}}\right),$$

where the right-hand side stands for the internal and kinetic energy input due to the fluid source θ.

3.3. Energy compatible time scheme

We propose here an energy-compatible time scheme. Instead of the scheme proposed by Gonzalez (2000) and used in the heart model of Chapelle et al. (2012) and in the poromechanical model of Chapelle and Moireau (2014), we draw our inspiration from Le Tallec and Hauret (2002) and use a mid-point Newmark scheme. We lose the exact energy conservation property, but mid-point schemes are easier to handle and allow us to get a second-order energy conservation. We propose the following time discretization of (14)

$$\begin{cases} (\rho_0 + m^{n+\frac{1}{2}})d_0 \frac{v^{n+1}-v^n}{\Delta t} + \left(1 + \frac{y^{n+\frac{1}{2}}}{R_0}\right)\frac{d_0}{R_0}\Sigma_{\text{sph}}^{n+\frac{1}{2}\sharp} \\ \quad = (\rho_0 + m^{n+\frac{1}{2}})d_0 f^{n+\frac{1}{2}} + P_v^{n+\frac{1}{2}}\left(1 + \frac{y^{n+\frac{1}{2}}}{R_0} - \frac{J^{n+\frac{1}{2}\sharp}d_0}{2R_0}\left(1 + \frac{y^{n+\frac{1}{2}}}{R_0}\right)^{-2}\right)^2 \\ \quad\quad \left(1 + J^{n+\frac{1}{2}\sharp}\frac{d_0}{R_0}\left(1 + \frac{y^{n+\frac{1}{2}}}{R_0}\right)^{-3}\right) \qquad \text{(a)} \\ \frac{y^{n+1}-y^n}{\Delta t} = v^{n+\frac{1}{2}}, \qquad \text{(b)} \\ \frac{m^{n+1}-m^n}{\Delta t} = J^{n+\frac{1}{2}\sharp}\theta^{n+\frac{1}{2}}, \qquad \text{(c)} \end{cases} \tag{19}$$

with, substituting (16)(c) into (16)(e), $\Sigma_{\text{sph}}^{n+\frac{1}{2}\sharp}$ and $J^{n+\frac{1}{2}\sharp}$ defined by the following two relations (we recall that $J_s = J - \frac{m}{\rho_f} - \phi_0$)

$$\begin{cases} \Sigma_{\text{sph}}^{n+\frac{1}{2}\sharp} = \left(\frac{\partial \Psi_e}{\partial \underline{\underline{e}}}\right)_{\phi_1\phi_1}(y^{n+\frac{1}{2}}, J^{n+\frac{1}{2}\sharp}) + \left(\frac{\partial \Psi_e}{\partial \underline{\underline{e}}}\right)_{\phi_2\phi_2}(y^{n+\frac{1}{2}}, J^{n+\frac{1}{2}\sharp}) \\ \quad -2(J^{n+\frac{1}{2}\sharp})^2 C(y^{n+\frac{1}{2}})^{-3}\left(\frac{\partial \Psi_e}{\partial \underline{\underline{e}}}\right)_{rr}(y^{n+\frac{1}{2}}, J^{n+\frac{1}{2}\sharp}) \\ \quad +\sigma_{1D}^{n+\frac{1}{2}}\left(1 + \lambda - 2\lambda(J^{n+\frac{1}{2}\sharp})^2 C(y^{n+\frac{1}{2}})^{-3}\right), \qquad \text{(a)} \\ -\frac{\partial \Psi_{\text{bulk}}}{\partial J_s}(J^{n+\frac{1}{2}\sharp} - \frac{m^{n+\frac{1}{2}}}{\rho_f} - \phi_0) \\ \quad = J^{n+\frac{1}{2}\sharp} C(y^{n+\frac{1}{2}})^{-2}\left(\frac{\partial \Psi_e}{\partial \underline{\underline{e}}}\right)_{rr}(y^{n+\frac{1}{2}}, J^{n+\frac{1}{2}\sharp}) \\ \quad\quad + \lambda J^{n+\frac{1}{2}\sharp} C(y^{n+\frac{1}{2}})^{-2}\sigma_{1D}^{n+\frac{1}{2}}. \qquad \text{(b)} \end{cases} \tag{20}$$

Remark 4 (*Solid Incompressibility*)**.** In the solid incompressibility limit, the use of $J^{n+\frac{1}{2}}$ is justified by the following relation that replaces (20)(b)

$$J^{n+\frac{1}{2}} = 1 + \frac{m^{n+\frac{1}{2}}}{\rho_f}. \tag{21}$$

In order to establish the compatibility of the scheme (19) with the energy balance derived in Section 3.2, we remove the loadings $f = 0$ and $P_v = 0$, the active contribution $\sigma_{1D} = 0$ and the solid damping $\eta = 0$. We look for a bound of our discrete energy with the fluid source term θ that we retain. Moreover, we perform the analysis in the specific case of an incompressible solid constituent, hence using (21), where the notation $J^{n+\frac{1}{2}}$ instead of $J^{n+\frac{1}{2}\sharp}$ is justified by the explicit affine relation that now links the variables J and m. Multiplying (19)(a) by $v^{n+\frac{1}{2}}$ and using (19)(c), the first term gives

$$\begin{aligned} &(\rho_0 + m^{n+\frac{1}{2}})\left(\frac{v^{n+1}-v^n}{\Delta t}\right)\left(\frac{v^{n+1}+v^n}{2}\right) = (\rho_0 + m^{n+\frac{1}{2}})\frac{(v^{n+1})^2 - (v^n)^2}{2\Delta t} \\ &= (\rho_0 + m^{n+1})\frac{(v^{n+1})^2}{2\Delta t} - (\rho_0 + m^n)\frac{(v^n)^2}{2\Delta t} \\ &\quad + \frac{m^n - m^{n+1}}{2}\frac{(v^{n+1})^2}{2\Delta t} - \frac{m^{n+1} - m^n}{2}\frac{(v^n)^2}{2\Delta t} \\ &= \frac{E_c^{n+1} - E_c^n}{\Delta t} - \frac{1}{2}J^{n+\frac{1}{2}}\theta^{n+\frac{1}{2}}\frac{(v^n)^2 + (v^{n+1})^2}{2}, \end{aligned} \tag{22}$$

with $E_c^n = \frac{1}{2}(\rho_0 + m_f^n)v^n$ the discrete kinetic energy.

To make the following derivations simpler, we express $\underline{\underline{e}}$ and $\underline{\underline{C}}$ in terms of J instead of the state variable m, according to the relation (21).

For the second term, we write that thanks to (19)(b),

$$\begin{aligned} &\left(1 + \frac{y^{n+\frac{1}{2}}}{R_0}\right)\frac{y^{n+1} - y^n}{R_0 \Delta t} \\ &= \frac{1}{\Delta t}\left[\left(\frac{y^{n+1}}{R_0} + \frac{(y^{n+1})^2}{2R_0^2}\right) - \left(\frac{y^n}{R_0} + \frac{(y^n)^2}{2R_0^2}\right)\right] = \frac{e^{n+1} - e^n}{\Delta t}, \end{aligned} \tag{23}$$

with $e^n = (\underline{\underline{e}}(y^n, J^n))_{\phi_1\phi_1} = (\underline{\underline{e}}(y^n, J^n))_{\phi_2\phi_2}$ that depends only on y^n. With $\underline{\underline{e}}^n = \underline{\underline{e}}(y^n, J^n)$ and $\underline{\underline{e}}^{n+\frac{1}{2}\sharp} = \underline{\underline{e}}(y^{n+\frac{1}{2}}, J^{n+\frac{1}{2}})$, we have the following Taylor expansions:

$$\begin{aligned} \Psi_e^{n+1} = \Psi_e(\underline{\underline{e}}^{n+1}) &= \Psi_e(\underline{\underline{e}}^{n+\frac{1}{2}\sharp}) + (\underline{\underline{e}}^{n+1} - \underline{\underline{e}}^{n+\frac{1}{2}\sharp}) : \frac{\partial \Psi_e}{\partial \underline{\underline{e}}}(\underline{\underline{e}}^{n+\frac{1}{2}\sharp}) \\ &\quad + \frac{1}{2}(\underline{\underline{e}}^{n+1} - \underline{\underline{e}}^{n+\frac{1}{2}\sharp})^2 : \frac{\partial^2 \Psi_e}{\partial \underline{\underline{e}}^2}(\underline{\underline{e}}^{n+\frac{1}{2}\sharp}) \\ &\quad + O((\underline{\underline{e}}^{n+1} - \underline{\underline{e}}^{n+\frac{1}{2}\sharp})^3), \\ \Psi_e^n = \Psi_e(\underline{\underline{e}}^n) &= \Psi_e(\underline{\underline{e}}^{n+\frac{1}{2}\sharp}) - (\underline{\underline{e}}^{n+\frac{1}{2}\sharp} - \underline{\underline{e}}^n) : \frac{\partial \Psi_e}{\partial \underline{\underline{e}}}(\underline{\underline{e}}^{n+\frac{1}{2}\sharp}) \\ &\quad + \frac{1}{2}(\underline{\underline{e}}^{n+\frac{1}{2}\sharp} - \underline{\underline{e}}^n)^2 : \frac{\partial^2 \Psi_e}{\partial \underline{\underline{e}}^2}(\underline{\underline{e}}^{n+\frac{1}{2}\sharp}) + O((\underline{\underline{e}}^{n+\frac{1}{2}\sharp} - \underline{\underline{e}}^n)^3), \end{aligned}$$

and

$$\begin{aligned} \underline{\underline{e}}^{n+1} - \underline{\underline{e}}^{n+\frac{1}{2}\sharp} &= d_y \underline{\underline{e}}(y^{n+\frac{1}{2}}, J^{n+\frac{1}{2}}) \cdot \frac{y^{n+1} - y^n}{2} + d_J \underline{\underline{e}}(y^{n+\frac{1}{2}}, J^{n+\frac{1}{2}}) \cdot \frac{J^{n+1} - J^n}{2} \\ &\quad + O(((J^{n+1} - J^n), (y^{n+1} - y^n))^2), \\ \underline{\underline{e}}^{n+\frac{1}{2}\sharp} - \underline{\underline{e}}^n &= d_y \underline{\underline{e}}(y^{n+\frac{1}{2}}, J^{n+\frac{1}{2}}) \cdot \frac{y^{n+1} - y^n}{2} + d_J \underline{\underline{e}}(y^{n+\frac{1}{2}}, J^{n+\frac{1}{2}}) \cdot \frac{J^{n+1} - J^n}{2} \\ &\quad + O(((J^{n+1} - J^n), (y^{n+1} - y^n))^2). \end{aligned}$$

Assuming that $d_y \underline{\underline{e}}$ and $d_J \underline{\underline{e}}$ are bounded, by subtraction,

$$\Psi_e^{n+1} - \Psi_e^n = (\underline{\underline{e}}^{n+1} - \underline{\underline{e}}^n) : \frac{\partial \Psi_e}{\partial \underline{\underline{e}}}(\underline{\underline{e}}^{n+\frac{1}{2}\sharp}) + O(((y^{n+1} - y^n), (J^{n+1} - J^n))^3).$$

From now on we assume that $O(y^{n+1} - y^n) = O(J^{n+1} - J^n) = O(\Delta t)$, then

$$\begin{aligned} \frac{\Psi_e^{n+1} - \Psi_e^n}{\Delta t} &= \frac{e_{rr}^{n+1} - e_{rr}^n}{\Delta t}\left(\frac{\partial \Psi_e}{\partial \underline{\underline{e}}}\right)_{rr}(\underline{\underline{e}}^{n+\frac{1}{2}\sharp}) \\ &+ \frac{e^{n+1} - e^n}{\Delta t}\left[\left(\frac{\partial \Psi_e}{\partial \underline{\underline{e}}}\right)_{\phi_1\phi_1}(\underline{\underline{e}}^{n+\frac{1}{2}\sharp}) + \left(\frac{\partial \Psi_e}{\partial \underline{\underline{e}}}\right)_{\phi_2\phi_2}(\underline{\underline{e}}^{n+\frac{1}{2}\sharp})\right] + O(\Delta t^2), \end{aligned} \tag{24}$$

with $e_{rr}^n = (\underline{\underline{e}}^n)_{rr}$ so that

$$e_{rr}^{n+1} - e_{rr}^n = \frac{1}{2}\left(\frac{(J^{n+1})^2}{C(y^{n+1})^2} - \frac{(J^n)^2}{C(y^n)^2}\right).$$

Again, Taylor expansions give

$$\begin{aligned} \frac{(J^{n+1})^2}{C(y^{n+1})^2} &= \frac{(J^{n+\frac{1}{2}})^2}{C(y^{n+\frac{1}{2}})^2} \cdot \left(1 + \frac{J^{n+1} - J^n}{J^{n+\frac{1}{2}}} + \left(\frac{J^{n+1} - J^n}{2J^{n+\frac{1}{2}}}\right)^2\right) \\ &\quad \cdot \left[1 + \frac{C'(y^{n+\frac{1}{2}})}{C(y^{n+\frac{1}{2}})}(y^{n+1} - y^n) \right. \\ &\quad \left. + \left(\frac{C''(y^{n+\frac{1}{2}})}{C(y^{n+\frac{1}{2}})} + \frac{C'(y^{n+\frac{1}{2}})^2}{C(y^{n+\frac{1}{2}})^2}\right)\frac{(y^{n+1} - y^n)^2}{4} + O(\Delta t^3)\right]^{-1} \\ &= \frac{(J^{n+\frac{1}{2}})^2}{C(y^{n+\frac{1}{2}})^2}\left[1 + \frac{J^{n+1} - J^n}{J^{n+\frac{1}{2}}} - \frac{C'(y^{n+\frac{1}{2}})}{C(y^{n+\frac{1}{2}})}(y^{n+1} - y^n)\right. \\ &\quad + \left(\frac{J^{n+1} - J^n}{2J^{n+\frac{1}{2}}}\right)^2 - \frac{C'(y^{n+\frac{1}{2}})}{J^{n+\frac{1}{2}}C(y^{n+\frac{1}{2}})}(y^{n+1} - y^n)(J^{n+1} - J^n) \\ &\quad \left. - \left(\frac{C''(y^{n+\frac{1}{2}})}{C(y^{n+\frac{1}{2}})} + \frac{C'(y^{n+\frac{1}{2}})^2}{C(y^{n+\frac{1}{2}})^2}\right)\frac{(y^{n+1} - y^n)^2}{4} + O(\Delta t^3)\right], \end{aligned}$$

Δt	C_0, C_2	C_1, C_3	C_4	ρ_0, ρ_f	R_0	d	λ
1e-3	500	0.6	26000	1000	0.02	0.014	0.44
k_{ca}, k_{cv}	R_p	C_p	R_d	C_d	R_c	C_c	P_{sv}
2e-6	1.7e7	2.35e-10	1.55e8	1.1e-8	1.7e7	8.5e-11	500
σ_0	k_0	α	η	μ_c	K_{at}	K_p	K_{ar}
55e3	2.95e5	1.5	70	70	9e-6	5e-10	1.3e-5

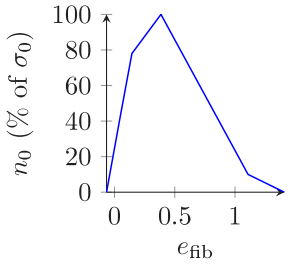

Fig. 4. Main parameters of the model in healthy heart simulation and the Frank–Starling mechanism function n_0 modulating the active stress σ_0 developed by the sarcomere with respect to the myocardial fiber extension e_{fib}. All units are in SI.

and similarly

$$\frac{(J^n)^2}{C(y^n)^2} = \frac{(J^{n+\frac{1}{2}})^2}{C(y^{n+\frac{1}{2}})^2}\left[1 - \frac{J^{n+1}-J^n}{J^{n+\frac{1}{2}}} + \frac{C'(y^{n+\frac{1}{2}})}{C(y^{n+\frac{1}{2}})}(y^{n+1}-y^n) + \left(\frac{J^{n+1}-J^n}{2J^{n+\frac{1}{2}}}\right)^2 - \frac{C'(y^{n+\frac{1}{2}})}{J^{n+\frac{1}{2}}C(y^{n+\frac{1}{2}})}(y^{n+1}-y^n)(J^{n+1}-J^n) - \left(\frac{C''(y^{n+\frac{1}{2}})}{C(y^{n+\frac{1}{2}})} + \frac{C'(y^{n+\frac{1}{2}})^2}{C(y^{n+\frac{1}{2}})^2}\right)\frac{(y^{n+1}-y^n)^2}{4} + O(\Delta t^3)\right],$$

Using that $C'(y^{n+\frac{1}{2}}) = 2e'(y^{n+\frac{1}{2}})$ and that

$$e'(y^{n+\frac{1}{2}})(y^{n+1}-y^n) = e^{n+1}-e^n + O(\Delta t^3),$$

this allows us to write

$$e_{rr}^{n+1} - e_{rr}^n = \frac{(J^{n+\frac{1}{2}})^2}{C(y^{n+\frac{1}{2}})^2}\left(\frac{J^{n+1}-J^n}{J^{n+\frac{1}{2}}} - 2\frac{e^{n+1}-e^n}{C(y^{n+\frac{1}{2}})} + O(\Delta t^3)\right).$$

Finally, (24) can be rewritten as

$$\frac{\Psi_e^{n+1}-\Psi_e^n}{\Delta t} = \frac{e^{n+1}-e^n}{\Delta t}\left[\left(\frac{\partial \Psi_e}{\partial \underline{\underline{e}}}\right)_{\phi_1\phi_1}(\underline{\underline{e}}^{n+\frac{1}{2}\sharp}) + \left(\frac{\partial \Psi_e}{\partial \underline{\underline{e}}}\right)_{\phi_2\phi_2}(\underline{\underline{e}}^{n+\frac{1}{2}\sharp}) - 2\frac{(J^{n+\frac{1}{2}})^2}{C(y^{n+\frac{1}{2}})^3}\left(\frac{\partial \Psi_e}{\partial \underline{\underline{e}}}\right)_{rr}(\underline{\underline{e}}^{n+\frac{1}{2}\sharp})\right] + \frac{J^{n+\frac{1}{2}}}{C(y^{n+\frac{1}{2}})^2}\frac{J^{n+1}-J^n}{\Delta t}\left(\frac{\partial \Psi_e}{\partial \underline{\underline{e}}}\right)_{rr}(\underline{\underline{e}}^{n+\frac{1}{2}\sharp}) + O(\Delta t^2).$$

Using (23) and (20)(a), the second term of the multiplication of (19) by $v^{n+\frac{1}{2}}$ gives

$$\frac{\Psi_e^{n+1}-\Psi_e^n}{\Delta t} - \frac{J^{n+\frac{1}{2}}}{C(y^{n+\frac{1}{2}})^2}\frac{J^{n+1}-J^n}{\Delta t}\left(\frac{\partial \Psi_e}{\partial \underline{\underline{e}}}\right)_{rr}(\underline{\underline{e}}^{n+\frac{1}{2}\sharp}) + O(\Delta t^2)$$

and, using also (22), (19)(c) and (21), we end up with the following discrete energy balance, for $\mathcal{E}^n = E_c^n + \Psi_e^n$ – we recall that the incompressible solid does not store any energy in Ψ_{bulk} –

$$\frac{\mathcal{E}^{n+1}-\mathcal{E}^n}{\Delta t} = J^{n+\frac{1}{2}}\theta^{n+\frac{1}{2}}\left[\frac{(v^n)^2+(v^{n+1})^2}{4} + \frac{p^{n+\frac{1}{2}\sharp}}{\rho_f}\right] + O(\Delta t^2),$$

with the discrete pressure

$$p^{n+\frac{1}{2}\sharp} = \frac{J^{n+\frac{1}{2}}}{C(y^{n+\frac{1}{2}})^2}\left(\frac{\partial \Psi_e}{\partial \underline{\underline{e}}}\right)_{rr}(\underline{\underline{e}}^{n+\frac{1}{2}\sharp}).$$

This second-order energy conservation is consistent with Le Tallec and Hauret (2002) and justifies our mid-point discretizations. Note that further refinement inspired from Gonzalez (2000) should allow to have an exact energy balance at the discrete level as obtained in the non-perfused 0D cardiac model in (Manganotti et al., 2021). We also refer to Manganotti et al. (2021) for the time-discretization choices adapted to the valve and circulation models considered in the present work.

4. Numerical simulations

The cost-effectiveness of the proposed 0D poromechanical model and its relative simplicity of use make it a useful tool when trying to simulate various physiological situations. In this section, we first perform the simulations of contraction and myocardial perfusion of a healthy heart at rest and after maximum vasodilation in the coronary network, motivated by clinically used adenosine stress tests. Secondly, we consider the stenosis of a large coronary artery and assess typical physiological indicators used in cardiology. Then, we modify the properties of the porous medium to mimic diseases affecting the microcirculation. Finally, we consider the effect of inotropic activation in the simulations.

4.1. Healthy heart simulation

We assume the incompressibility of the solid constituent, and the hyperelastic potential Ψ_e is in the form

$$\Psi_e = C_0\exp(C_1(J_1-3)^2) + C_2\exp(C_3(J_4-1)^2) + C_4(J_3 - 1 - \ln J_3).$$

We use the time scheme described in Section 3.3, and the parameters listed in Fig. 4. These parameters were calibrated to reproduce a realistic simulation of a healthy heart at rest according to the following criteria:

- the volume fraction of perfusion blood within the myocardium being 12 to 15% (Spaan, 1985);
- the myocardial perfusion flux being 1mL/s/100 g of myocardial tissue (Kajander et al., 2011) (in our myocardium, the weight of the left ventricle is 130 g and the target value in our calibration is therefore 1.3 mL/s);

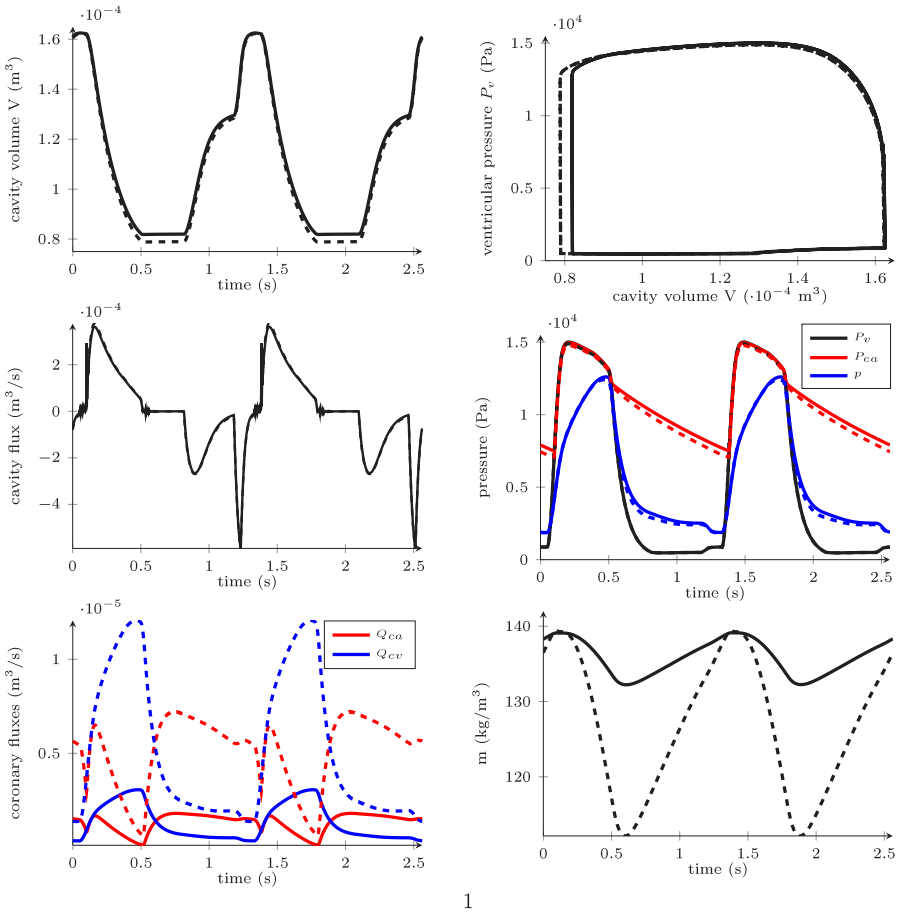

Fig. 5. Cardiac cycle of a healthy case obtained with the 0D model. The solid lines represent a healthy heart at rest ($F_{\text{micro}} = 1$) and the dashed lines correspond to the results with the assumed maximum vasodilation in adenosine-stress test (i.e., $F^{\text{vd}}_{\text{micro}} = 4$). (For interpretation of the references to color in this figure legend, the reader is referred to the web version of this article.)

- the simulated stroke volume, aortic pressure and flux having been previously calibrated in the model with respect to measured clinical data by Le Gall et al. (2020).

We plot the cavity flux, the perfusion mass m, the perfusion, cavity and coronary artery pressures and the coronary artery and venous fluxes

$$Q_{ca} = V_{myo}\, k_{ca}(P_{ca} - p) \quad \text{and} \quad Q_{cv} = V_{myo}\, k_{cv}(p - P_{cv}).$$

In Fig. 5, the perfusion mass and pressure show the systolic flow impediment: blood is drained out of the myocardium during the contraction (systole), and coronary circulation is reestablished during the relaxation (diastole).

The coronary vasodilation – a decrease of vascular resistance by vasodilation of small arteries, arterioles, venules and small veins – is in the proposed model represented by an increase of the conductances k_{ca} (arterial vasodilation) and k_{cv} (venous vasodilation). In order to objectively define this phenomenon, we consider that the microvascular coronary conductances k_{ca} and k_{cv}, as calibrated at rest, are multiplied by a factor spanning an interval between F_{micro} and $F^{\text{vd}}_{\text{micro}}$, corresponding to the basal vascular tone ("basal vasodilation") and maximum coronary vasodilation, respectively, with $F_{\text{micro}} = 1$ for our healthy heart at rest. According to Chilian et al. (1989), we assume that the conductance in the microcirculation of a healthy heart at maximum coronary vasodilation can increase fourfold, i.e., $F^{\text{vd}}_{\text{micro}} = 4F_{\text{micro}}$.

Fig. 5 shows the heart perfusion at baseline and at maximum vasodilation, and illustrates that the healthy heart can increase the perfusion flow by approximately a factor 4 — the so-called Coronary Flow Reserve (CFR) (Gould et al., 1990), defined as the ratio of the mean coronary flow at maximum vasodilation to that at baseline, see Table 1. To obtain the CFR value from our numerical experiments, we post-processed the simulation results and computed

$$\text{CFR} = \overline{Q_a\big(\max(F^{\text{vd}}_{\text{micro}})\big)} \big/ \overline{Q_a(\text{baseline})}, \tag{25}$$

where $\overline{\varphi}$ stands for the mean in time of a physical quantity φ. In every case (including pathological cases in next sections), we assume that the patient at rest reaches $\overline{Q_a(\text{baseline})} = 1.33$ mL/s (as calibrated and assumed from the normal myocardial perfusion flux, in order to keep the myocardial function at rest normal). This would typically be achieved by a certain level of vasodilation even at rest (thus reducing the perfusion reserve). In all cases – including in the pathological ones – we will assume that $\max(F^{\text{vd}}_{\text{micro}}) = 4F_{\text{micro}}$. In particular, for the healthy case (25) reads $\text{CFR} = \overline{Q_a(F^{\text{vd}}_{\text{micro}} = 4)} \big/ \overline{Q_a(\text{baseline})}$.

4.2. Large coronary artery stenosis

A stenosis, an abnormal narrowing of blood vessel, is in the coronaries typically due to the atherosclerosis (fatty deposits in the vessel wall) (Mann et al., 2014). In order to reproduce a macrovascular coronary stenosis in our model, we introduce a factor F_{sten} that multiplies the resistance of large coronary arteries R_c in the Windkessel component (8) (and divide the capacitance C_c by the same factor to keep the R_cC_c time constant), see Fig. 6. In our calibrated model, a healthy heart corresponds to $F_{\text{sten}} = 1$, whereas a moderate and severe stenosis would correspond to $F_{\text{sten}} = 40$, $F_{\text{sten}} = 100$, respectively. The basal and maximum vasodilation during the adenosine stress test, under the assumption of a normal microcirculation, are given by $F_{\text{micro}} = 1$,

Table 1
Numerical results corresponding to healthy case ($F_{\text{sten}} = 1$) and stenosis of large coronary artery of two levels ($F_{\text{sten}} = 40$ and 100) at rest and adenosine-stress test (relative microvascular resistances being $F_{\text{micro}}, F^{\text{vd}}_{\text{micro}}$ 1 and 4, respectively), from the simulations depicted in Figs. 5 and 7. In each case we compute the increase of blood mass per cycle (Δm) and the mean arterial flow ($\overline{Q_a}$). We also derive the indicators of fractional and coronary flow reserve (FFR and CFR, defined at maximum vasodilation). Note that CFR can decrease by a factor two in a severe stenosis.

$F_{\text{micro}}, F^{\text{vd}}_{\text{micro}}$	F_{sten}	Δm (kg/m^3)	$\overline{Q_a}$ (mL/s)	FFR	CFR
1	1	6.8	1.33		
4	1	27	5.16	1	3.9
1	40	6.6	1.22		
4	40	24	3.74	0.76	2.8
1	100	6.4	1.07		
4	100	21	2.58	0.56	1.9

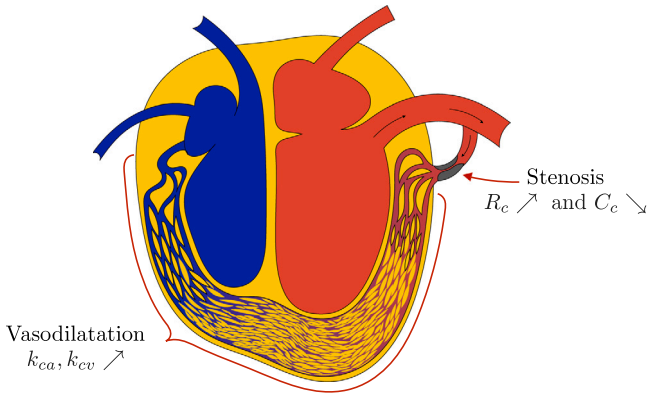

Fig. 6. Coronary vasodilation and stenosis. To model coronary vasodilation, the microvascular conductances k_{ca} and k_{cv} are multiplied by a factor $F^{\text{vd}}_{\text{micro}} > 1$. To reproduce a macrovascular coronary stenosis, the resistance R_c in the Windkessel model is multiplied by a factor F_{sten} that goes up to 100 in our illustrative simulations. (For interpretation of the references to color in this figure legend, the reader is referred to the web version of this article.)

$F^{\text{vd}}_{\text{micro}} = 4F_{\text{micro}}$, respectively, as in the physiological case (Section 4.1). Fig. 7 shows the simulation results of these two levels of macrovascular coronary artery stenosis. In comparison with the healthy case (Fig. 5), we can observe the progressively decreasing maximum flux in the coronary arteries at maximum vasodilation (dashed red lines during diastole), suggesting a decreasing myocardial perfusion reserve.

To better assess the severity of a large coronary artery stenosis than by a simple geometrical measurement (Fischer et al., 2002), the current gold standard functional measurements rely on the ratio of its downstream to upstream mean pressures assessed at maximum vasodilation induced by adenosine, i.e., the so-called Fractional Flow Reserve (FFR) (introduced by Pijls et al. (1993)). The value FFR ≈ 0.8 characterizes ischemia for which the intervention would have a limited effect. On the contrary, FFR < 0.75 suggests an ischemia for which the risk-benefit ratio is in favor of intervention (e.g. stenting) (Bech et al., 2001; Pijls et al., 2007). Due to the usefulness of the FFR concept, we post-processed the results of our simulations and computed FFR $= \overline{P_{ca}}/\overline{P_{ar}}$.

Table 1 summarizes these results. We can see that, for example, in our most severe stenosis case ($F_{\text{sten}} = 100$), the level of coronary vasodilation would have to be increased even at rest to keep a viable myocardium perfusion flux (of around 1.3 mL/s), which would then decrease the potential of further dilation at exercise (i.e., a decreased contractile reserve).

While FFR $= 0.76$ for $F_{\text{sten}} = 40$ signifies a borderline stenosis, FFR $= 0.56$ for $F_{\text{sten}} = 100$ suggests an indication for intervention.

4.3. Microvascular disease and combination of micro- and macrovascular involvement

In parallel with a narrowing in large coronary arteries (macrovascular stenosis), the microvessels can be affected by a pathological process (microvascular disease) (Arthur et al., 2012). In our model, the microvascular disease corresponds to decreased microvascular conductances k_{ca} and k_{cv} for basal vasodilation (therefore, $F_{\text{micro}} < 1$ with the small vessel conductance factor F_{micro} as defined in Section 4.1). Then, the maximum achievable vasodilation with the adenosine-stress test would be within our assumptions $\max(F^{\text{vd}}_{\text{micro}}) = 4F_{\text{micro}} < 4$.

Typically, the ischemic heart disease of a given patient has both components – stenosis of large coronaries and microvascular disease – in varying proportions. We performed a set of simulations combining macrovascular stenosis (up to severe stenosis with the resistance of large coronaries increased by a factor $F_{\text{sten}} = 100$) and microvascular disease, in which we decreased the conductance of the microvessel compartment down to $F_{\text{micro}} = 0.4$ (relatively to the healthy case).

In Fig. 8, we plot the mean arterial flow in the coronaries, together with CFR and FFR, for different values of $(F^{\text{vd}}_{\text{micro}}, F_{\text{sten}})$. Each curve corresponds to a microvascular state F_{micro} (with or without vasodilation), and the abscissa corresponds to the macrovascular stenosis F_{sten} simulated. For example, for a given microcirculation state $F^{\text{vd}}_{\text{micro}}$, moving along a curve leftwards can be interpreted as "virtual stenting". This illustrates the limit of the single FFR indicator when evaluating the relevance of stenting: for example, if the microvascular circulation is affected, stenting can bring FFR to 1, but does not always sufficiently improve CFR.

To overcome the limit of such a simple functional index as FFR, the perfusion model offers other quantities such as $\overline{m}$, see Fig. 8, indirectly accessible by non-invasive imaging (e.g. perfusion MRI or positron emission tomography) (Morton et al., 2012).

4.4. Inotropic effect

In this section we perform a study on the effect of inotropic activation, i.e., increased heart contractility. The inotropic effect contributes to the physiological regulation (e.g. during exercise). In pathophysiology, a decreased cardiac output in HF can be compensated by a chronic inotropic activation (intrinsic or by pharmacotherapy). Increasing the generated active stresses in the myocardium will effectively increase the cardiac stroke volume. However, the negative counterpart lies in the reinforcement of the systolic flow impediment in the coronaries, which can make such an activation highly ineffective for an individual patient. Since our model of porous myocardium accounts for these interactions, it could be well-suited in targeting personalized therapy.

Fig. 9 demonstrates the effect of inotropic activation (compared with baseline) on the strengthening of the systolic flow impediment in our simulations and shows a decrease of the mean fluid mass $\overline{m}$, as the larger stresses drain more blood out of the myocardium.

Fig. 10 provides a comparison of the effect of increased contractility and the combination of micro- / macrovascular stenosis (as in

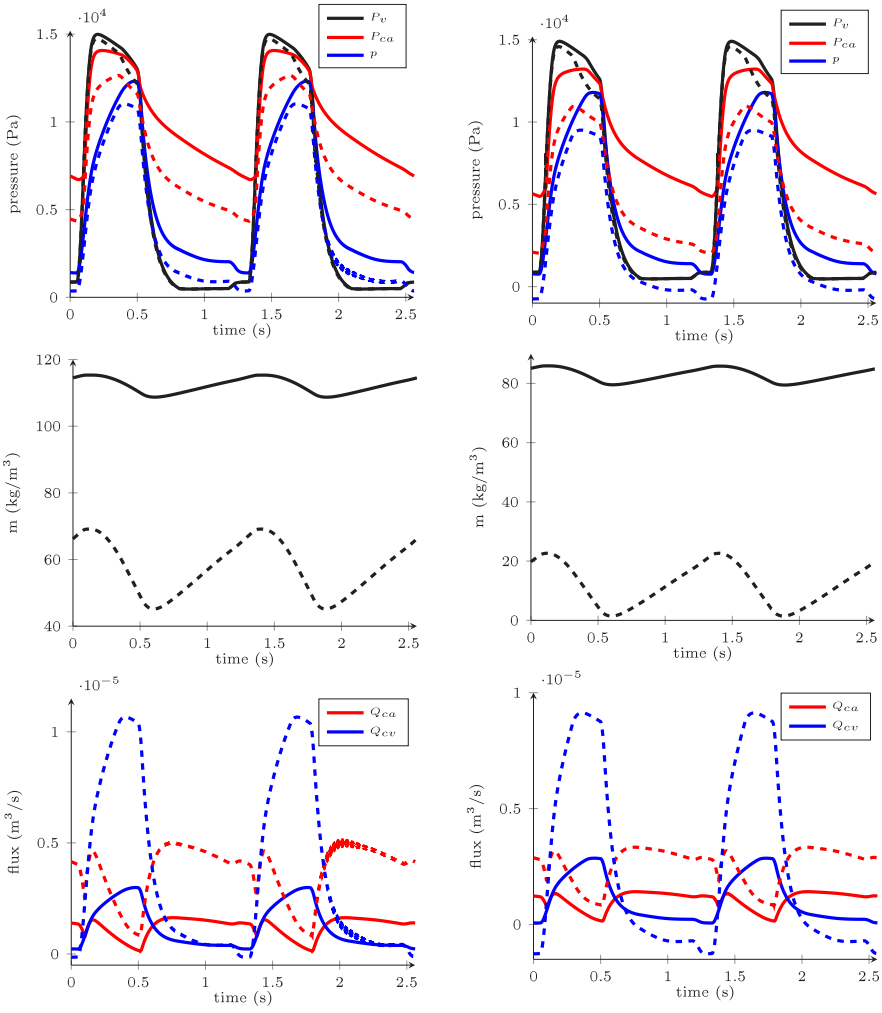

Fig. 7. Simulations with large coronary artery stenosis. The resistance of large coronary artery is increased by factor $F_{\text{sten}} = 40$ (left) and $F_{\text{sten}} = 100$ (right). Solid lines correspond to the situation at rest ($F_{\text{micro}} = 1$) and dashed lines to the maximum vasodilation in adenosine-stress test ($F^{\text{vd}}_{\text{micro}} = 4$). (For interpretation of the references to color in this figure legend, the reader is referred to the web version of this article.)

Section 4.3) on our set of indicators. The figure illustrates how the inotropic effect can compensate some microvascular diseases, strengthening the perfusion flow. For example, for $F^{\text{vd}}_{\text{micro}} = 3.2$, the contractility increased by a factor 1.5 almost re-establishes the output flow corresponding to $F^{\text{vd}}_{\text{micro}} = 4$. In the meantime, a higher flow and a better circulation reduce the mean fluid mass $\overline{m}$.

The increase of cardiac output given by a stronger muscular activity is accompanied by a boost in oxygen and nutrients demand within the myocardium. For further interpretation, and in order to evaluate the efficiency of this process, we would need to counterbalance the gain in the cardiac output according to the increase in perfusion demand. Our results show that the model gives promising qualitative reproductions of complex and coupled physiological phenomena, and this paves the way for future quantitative study using clinical or experimental data.

5. Limitations

Various limitations can be emphasized. The spherical symmetry assumption for the left ventricle is a rather drastic approximation, albeit it was demonstrated in (Caruel et al., 2014) that the resulting 0D model provides some very realistic physiological indicators of the cardiac behavior. This assumption is clearly incompatible with the modeling of pathological scenarios associated with spatial inhomogeneities, e.g. in the presence of ischemic or infarcted areas. However, such a geometrical model reduction could be useful when considering the patients with LV perfusion affected globally, as for instance patients with non-ischemic cardiomyopathies, after cardiotoxic chemotherapy for cancer treatment or after heart transplantation, particularly for the long-term monitoring of the progress of their microvascular disease. The approach has the potential to be incorporated in the analysis of non-invasive perfusion MRI as well as in the assessment of perfusion by invasive techniques (Pijls et al., 1993) to augment the information from these exams.

There are a number of challenges in constitutive models of living tissues. Some of them, concerning the modeling of arterial tissue, are discussed for example in (Rajagopal and Rajagopal, 2020; Myneni and Rajagopal, 2022). Experimental data of perfused myocardial tissue could allow to improve the proposed model.

The complex problem of interaction between the coronary circulation and myocardial contraction is further complicated by the interaction of blood with the biologically highly active inner cellular layer of blood vessels — endothelium. While the mechanobiology and biochemistry of endothelial cells, see e.g. (Dessalles et al., 2021; Lerman et al., 1995; Gimbrone Jr. and García-Cardeña, 2016), are out of the scope of the present paper, the endothelial dysfunction plays a substantial role in the development of coronary arterial disease and pathophysiology of myocardial perfusion and will be considered in future works. Furthermore, the inflow into the coronary arteries may be affected by the flow pattern in the aortic root and reliable models of

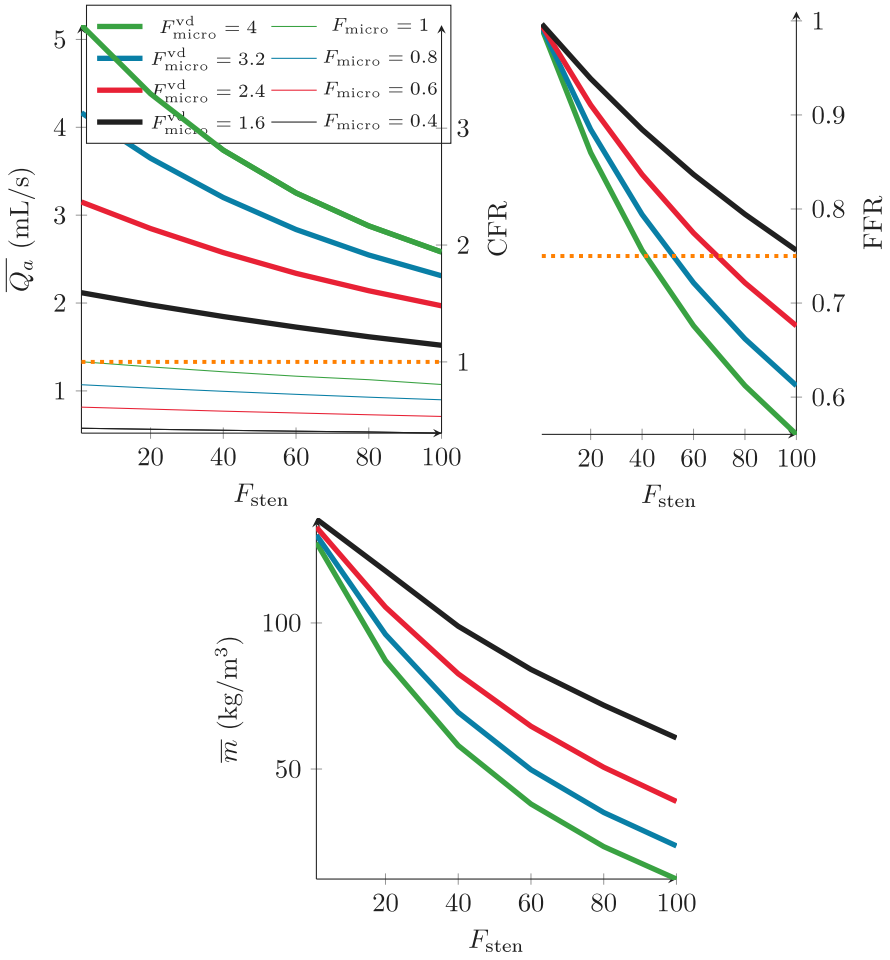

Fig. 8. Main indicators for micro- / macrovascular diseases. The coronary artery flow $\overline{Q_a}$ is plotted as a function of relative resistance of large coronary artery (F_{sten}), with additional quantities of Coronary Flow Reserve (CFR), Fractional Flow Reserve (FFR) and mean fluid mass $\overline{m}$. The thick lines correspond to the maximal vasodilation (each color for different microvascular state from normal $F_{micro} = 1$ down to severe microvascular disease $F_{micro} = 0.4$). The thin lines show the hypothetical situation without vasodilation. Note that in order to provide the minimum coronary flow necessary for myocardial metabolism (dashed orange line), the coronary circulation must be partially vasodilated even at rest. (For interpretation of the references to color in this figure legend, the reader is referred to the web version of this article.)

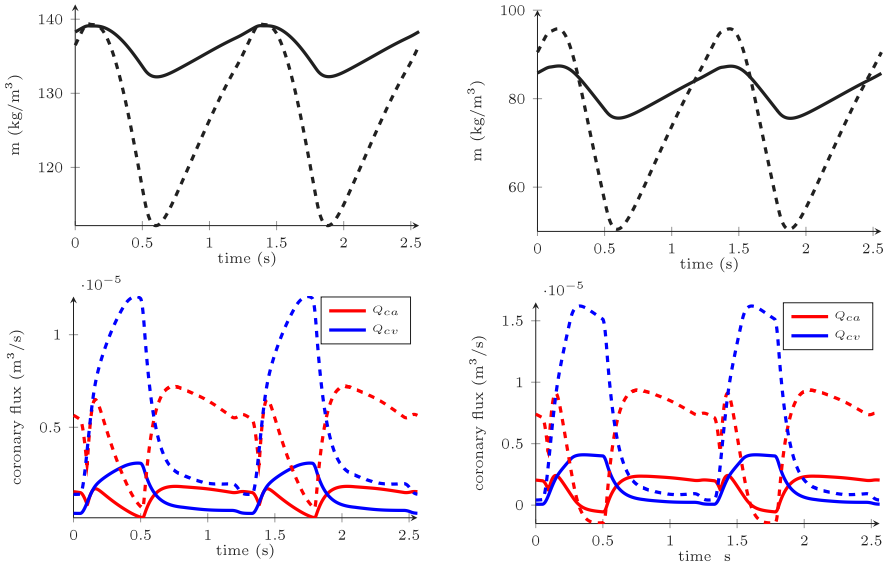

Fig. 9. Baseline (left) versus inotropic activation (i.e. contractility σ_0 increased by factor 1.5, on the right). We compare the added fluid mass m (at the top) and the coronary fluxes (at the bottom). In solid lines $F_{micro} = 1$, whereas dashed lines give the results with vasodilation $F^{vd}_{micro} = 4$. (For interpretation of the references to color in this figure legend, the reader is referred to the web version of this article.)

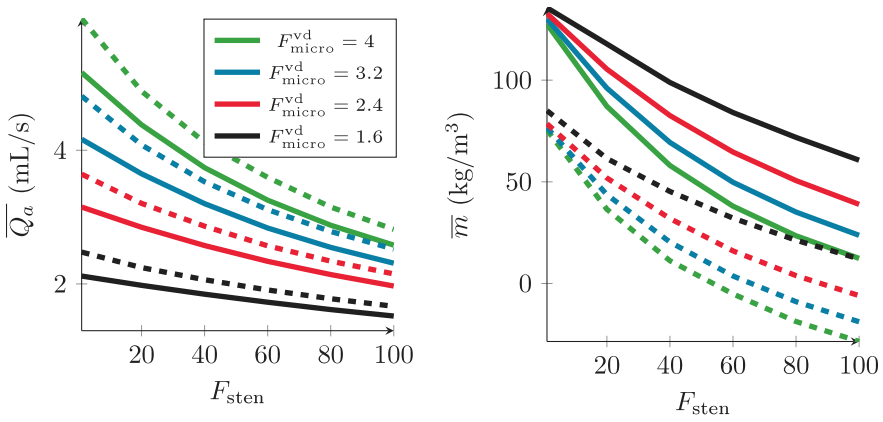

Fig. 10. Main indicators for micro/macro vascular diseases, study of the inotropic effect. As a function of F_{sten}, we plot the mean arterial coronary flow (and CFR, on the left) and the mean fluid mass (on the right), at maximal vasodilation. Each color corresponds to a microvascular state, solid lines represent a normal heart, whereas dashed lines represent an inotropic heart. (For interpretation of the references to color in this figure legend, the reader is referred to the web version of this article.)

large-vessel flow are therefore essential also for the microvascular flow modeling. The vorticity of the flow in the aortic root is hypothesized to play a significant role particularly in aortic valve disease (Boon, 2009; David, 2016) and the modeling works such as (Fučík et al., 2020; Chabiniok et al., 2022) may contribute toward the characterization of this component of the myocardial perfusion.

6. Conclusion

To conclude, extending (Chapelle et al., 2012), we have derived here a complete 3D cardiac model that now takes into account the myocardium perfusion and links the coronary circulation to the previous circulation model.

Drawing our inspiration from Caruel et al. (2014), we then performed a dimensional reduction to write a 0D perfused heart model. It allowed us to model new physical quantities (the perfusion mass and pressure) and to reproduce phenomena such as the flow impediment that occurs in systole, and the vasodilation that enables cardiac activity adaptation. We also illustrated the relevance of such improvements by reproducing coronary vascular diseases that represent a wide majority of heart diseases, and that could not be explained with previous models. The porous model accounts for the mechanical interactions between the coronary circulation and the myocardium activity, and allows qualitatively illustrating the inotropic effect.

As in (Caruel et al., 2014), this approach was motivated by the computational efficiency of 0D simulations, which have again proven to be very effective, reproducing quickly and faithfully complex physiological phenomena. A cardiac cycle is computed in about one minute with a standard computer, and we can consider using this model for physiological monitoring over a period of time. Nevertheless, here the limiting factor in cost-efficiency was the first guess of the initial state. Indeed, the heart cycle does not contain an equilibrium state and the initial state cannot be calculated as the solution of a static problem, as it is often made in dynamical simulations. Therefore, the computation of numerous cycles (here about 50) is necessary in order to reach the actual periodic cycle, and this warrants further research to optimize this process.

Further perspectives could also include quantitative studies of these physiological processes and other types of activation (e.g. chronotropy), other disorders e.g. in electrical activation, and an investigation of the dependence of the muscle cellular activity on the nutrients and oxygen supply. The proposed model could also be used for the calibration of more complex 3D cardiac models.

Declaration of competing interest

The authors declare that they have no known competing financial interests or personal relationships that could have appeared to influence the work reported in this paper.

Data availability

No data was used for the research described in the article.

Acknowledgment

We are grateful to Dr. Fabrice Vallée, Anesthesiology and Intensive Care Department, Lariboisière - Saint Louis - Fernand Widal University Hospitals, Paris, France, for several valuable discussions.

References

Arthur, H.M., Campbell, P., Harvey, P.J., McGillion, M., Oh, P., Woodburn, E., Hodgson, C., 2012. Women, cardiac syndrome X, and microvascular heart disease. Can. J. Cardiol. 28 (2), S42–S49. http://dx.doi.org/10.1016/j.cjca.2011.09.006.

Atkin, R.J., Craine, R.E., 1976a. Continuum theories of mixtures: basic theory and historical development. Quart. J. Mech. Appl. Math. 29 (2), 209–244.

Atkin, R.J., Craine, R.E., 1976b. Continuum theories of mixtures: applications. IMA J. Appl. Math. 17 (2), 153–207.

Bech, G.J.W., De Bruyne, B., Pijls, N.H.J., de Muinck, E.D., Hoorntje, J.C.A., Escaned, J., Stella, P.R., Boersma, E., Bartunek, J., Koolen, J.J., Wijns, W., 2001. Fractional flow reserve to determine the appropriateness of angioplasty in moderate coronary stenosis a randomized trial. Circulation 103 (24), 2928–2934.

Bestel, J., Clément, F., Sorine, M., 2001. A biomechanical model of muscle contraction. In: Medical Image Computing and Computer-Assisted Intervention - MICCAI 2001, Vol. 2208. (2), pp. 1159–1161.

Boon, B., 2009. Leonardo da Vinci on atherosclerosis and the function of the sinuses of Valsalva. Neth. Heart J. 17 (12), 496–499. http://dx.doi.org/10.1007/bf03086311.

Bowen, R.M., 1976. Theory of mixtures, vol. III. In: Continuum Physics: Mixtures and EM Field Theories. Academic Press, New York, pp. 1–127.

Bowen, R.M., 1980. Incompressible porous media models by use of the theory of mixtures. Internat. J. Engrg. Sci. (ISSN: 00207225) 18 (9), 1129–1148. http://dx.doi.org/10.1016/0020-7225(80)90114-7.

Caruel, M., Chabiniok, R., Moireau, P., Lecarpentier, Y., Chapelle, D., 2014. Dimensional reductions of a cardiac model for effective validation and calibration. Biomech. Model. Mechanobiol. 13 (4), 897–914.

Caruel, M., Moireau, P., Chapelle, D., 2019. Stochastic modeling of chemical–mechanical coupling in striated muscles. Biomech. Model. Mechanobiol. (ISSN: 1617-7959) 18 (3), 563–587. http://dx.doi.org/10.1007/s10237-018-1102-z.

Chabiniok, R., Hron, J., Jarolímová, A., Málek, J., Rajagopal, K.R., Rajagopal, K., Švihlová, H., Tůma, K., 2022. Three-dimensional flows of incompressible Navier-Stokes fluids in tubes containing a sinus, with varying slip conditions at the wall. Internat. J. Engrg. Sci. 180, 103749. http://dx.doi.org/10.1016/j.ijengsci.2022.103749.

Chabiniok, R., Wang, V.Y., Hadjicharalambous, M., Asner, L., Lee, J., Sermesant, M., Kuhl, E., Young, A.A., Moireau, P., Nash, M.P., Chapelle, D., Nordsletten, D.A., 2016. Multiphysics and multiscale modelling, data–model fusion and integration of organ physiology in the clinic: ventricular cardiac mechanics. Interface Focus 6 (2), 20150083.

Chapelle, D., Bathe, K.J., 2010. The Finite Element Analysis of Shells - Fundamentals. Springer Science & Business Media.

Chapelle, D., Gerbeau, J.F., Sainte-Marie, J., Vignon-Clementel, I.E., 2009. A poroelastic model valid in large strains with applications to perfusion in cardiac modeling. Comput. Mech. (ISSN: 0178-7675) 46 (1), 91–101. http://dx.doi.org/10.1007/s00466-009-0452-x, URL http://link.springer.com/10.1007/s00466-009-0452-x.

Chapelle, D., Le Tallec, P., Moireau, P., Sorine, M., 2012. Energy-preserving muscle tissue model: formulation and compatible discretizations. Int. J. Multiscale Comput. Eng. 10 (2).

Chapelle, D., Moireau, P., 2014. General coupling of porous flows and hyperelastic formulations-From thermodynamics principles to energy balance and compatible time schemes. Eur. J. Mech. B/Fluids (ISSN: 09977546) 46, 82–96. http://dx.doi.org/10.1016/j.euromechflu.2014.02.009, URL http://linkinghub.elsevier.com/retrieve/pii/S0997754614000302.

Chilian, W.M., Layne, S.M., Klausner, E.C., Eastham, C.L., Marcus, M.L., 1989. Redistribution of coronary microvascular resistance produced by dipyridamole. Am. J. Physiol.-Heart Circ. Physiol. 256 (2), H383–H390.

Coussy, O., 2004. Poromechanics. John Wiley & Sons.

David, T.E., 2016. Aortic valve sparing in different aortic valve and aortic root conditions. J. Am. Coll. Cardiol. 68 (6), 654–664. http://dx.doi.org/10.1016/j.jacc.2016.04.062.

Dessalles, C.A., Leclech, C., Castagnino, A., Barakat, A.I., 2021. Integration of substrate- and flow-derived stresses in endothelial cell mechanobiology. Commun. Biol. 4 (1), 1–15.

Fischer, J.J., Samady, H., McPherson, J.A., Sarembock, I.J., Powers, E.R., Gimple, L.W., Ragosta, M., 2002. Comparison between visual assessment and quantitative angiography versus fractional flow reserve for native coronary narrowings of moderate severity. Am. J. Cardiol. 90 (3), 210–215.

Fučík, R., Galabov, R., Pauš, P., Eichler, P., Klinkovský, J., Straka, R., Tintěra, J., Chabiniok, R., 2020. Investigation of phase-contrast magnetic resonance imaging underestimation of turbulent flow through the aortic valve phantom: Experimental and computational study using lattice Boltzmann method. Magn. Reson. Mater. Phys. Biol. Med. 33 (5), 649–662.

Gimbrone Jr., M.A., García-Cardeña, G., 2016. Endothelial cell dysfunction and the pathobiology of atherosclerosis. Circ. Res. 118 (4), 620–636.

Gonzalez, O., 2000. Exact energy and momentum conserving algorithms for general models in nonlinear elasticity. Comput. Methods Appl. Mech. Engrg. (ISSN: 00457825) 190 (13–14), 1763–1783. http://dx.doi.org/10.1016/S0045-7825(00)00189-4, URL http://linkinghub.elsevier.com/retrieve/pii/S0045782500001894.

Gould, K.L., Kirkeeide, R.L., Buchi, M., 1990. Coronary flow reserve as a physiologic measure of stenosis severity. J. Am. Coll. Cardiol. 15 (2), 459–474.

Gusseva, M., Hussain, T., Hancock Friesen, C., Moireau, P., Tandon, A., Greil, G., Hasbani, K., Chapelle, D., Chabiniok, R., 2021. Biomechanical modeling to inform pulmonary valve replacement in tetralogy of Fallot patients after complete repair. Can. J. Cardiol. 37, 1798–1807. http://dx.doi.org/10.1016/j.cjca.2021.06.018.

Hall, J.E., Hall, M.E., 2020. Guyton and Hall Textbook of Medical Physiology E-Book. Elsevier Health Sciences.

Jerosch-Herold, M., Wilke, N., Stillman, A.E., Wilson, R.F., 1998. Magnetic resonance quantification of the myocardial perfusion reserve with a Fermi function model for constrained deconvolution. Med. Phys. 25 (1), 73–84.

Kajander, S.A., Joutsiniemi, E., Saraste, M., Pietilä, M., Ukkonen, H., Saraste, A., Sipilä, H.T., Teräs, M., Mäki, M., Airaksinen, J., Hartiala, J., Knuuti, J., 2011. Clinical value of absolute quantification of myocardial perfusion with ^{15}O-water in coronary artery disease. Circ. Cardiovasc. Imaging 4 (6), 678–684.

Kajiya, F., Kajiya, M., Morimoto, T., Iwasaki, T., Inai, Y., Hirota, M., Kiyooka, T., Morizane, Y., Miyasaka, T., Mohri, S., et al., 2007. Physiomics of coronary perfusion and cardiac pumping. In: Cardiac Perfusion and Pumping Engineering. World Scientific Publishing Co, pp. 1–15.

Kimmig, F., Chapelle, D., Moireau, P., 2019. Thermodynamic properties of muscle contraction models and associated discrete-time principles. Adv. Model. Simul. Eng. Sci. 6 (1), 1–38.

Klika, V., 2014. A guide through available mixture theories for applications. Crit. Rev. Solid State Mater. Sci. 39 (2), 154–174.

Le Gall, A., Vallée, F., Pushparajah, K., Hussain, T., Mebazaa, A., Chapelle, D., Gayat, E., Chabiniok, R., 2020. Monitoring of cardiovascular physiology augmented by a patient-specific biomechanical model during general anesthesia. A proof of concept study. PLoS One 15 (5), e0232830.

Le Tallec, P., Hauret, P., 2002. Energy conservation in fluid structure interactions. In: Y. Kuznetsov, O. Pironneau (Ed.), Numerical Methods for Scientific Computing / Variational Problems and Applications – CIMNE Barcelona.

Lee, J., Cookson, A., Chabiniok, R., Rivolo, S., Hyde, E., Sinclair, M., Michler, C., Sochi, T., Smith, N., 2015. Multiscale modelling of cardiac perfusion. In: Modeling the Heart and the Circulatory System. Springer, pp. 51–96.

Lerman, A., Holmes Jr., D.R., Bell, M.R., Garratt, K.N., Nishimura, R.A., Burnett Jr., J.C., 1995. Endothelin in coronary endothelial dysfunction and early atherosclerosis in humans. Circulation 92 (9), 2426–2431.

Loret, B., Simões, F.M.F., 2005. A framework for deformation, generalized diffusion, mass transfer and growth in multi-species multi-phase biological tissues. Eur. J. Mech. A Solids 24 (5), 757–781.

Manganotti, J., Caforio, F., Kimmig, F., Moireau, P., Imperiale, S., 2021. Coupling reduced-order blood flow and cardiac models through energy-consistent strategies: modeling and discretization. Adv. Model. Simul. Eng. Sci. 8 (1), 21. http://dx.doi.org/10.1186/s40323-021-00206-4.

Mann, D.L., Zipes, D.P., Libby, P., Bonow, R.O., 2014. Braunwald's Heart Disease: A Textbook of Cardiovascular Medicine. Elsevier Health Sciences.

Morton, G., Chiribiri, A., Ishida, M., Hussain, S.T., Schuster, A., Indermuehle, A., Perera, D., Knuuti, J., Baker, S., Hedström, E., Schleyer, P., O'Doherty, M., Barrington, S., Nagel, E., 2012. Quantification of absolute myocardial perfusion in patients with coronary artery disease: comparison between cardiovascular magnetic resonance and positron emission tomography. J. Am. Coll. Cardiol. 60 (16), 1546–1555.

Myneni, M., Rajagopal, K.R., 2022. Constitutive modeling of the mechanical response of arterial tissues. Appl. Eng. Sci. 100111.

Pijls, N.H.J., van Schaardenburgh, P., Manoharan, G., Boersma, E., Bech, J.W., van't Veer, M., Bär, F., Hoorntje, J., Koolen, J., Wijns, W., de Bruyne, B., 2007. Percutaneous coronary intervention of functionally nonsignificant stenosis: 5-year follow-up of the DEFER study. J. Am. Coll. Cardiol. 49 (21), 2105–2111.

Pijls, N.H.J., Van Son, J.A., Kirkeeide, R.L., De Bruyne, B.L.G.K., Gould, K.L., 1993. Experimental basis of determining maximum coronary, myocardial, and collateral blood flow by pressure measurements for assessing functional stenosis severity before and after percutaneous transluminal coronary angioplasty. Circulation 87 (4), 1354–1367.

Plein, S., Ryf, S., Schwitter, J., Radjenovic, A., Boesiger, P., Kozerke, S., 2007. Dynamic contrast-enhanced myocardial perfusion MRI accelerated with k-t SENSE. Magn. Reson. Med. 58 (4), 777–785. http://dx.doi.org/10.1002/mrm.21381.

Rajagopal, K.R., Rajagopal, K., 2020. Modeling of the aorta: complexities and inadequacies. Aorta 8 (04), 091–097.

Rajagopal, K.R., Tao, L., 1995. Mechanics of Mixtures, Vol. 35. World scientific.

Ruijsink, B., Zugaj, K., Wong, J., Pushparajah, K., Hussain, T., Moireau, P., Razavi, R., Chapelle, D., Chabiniok, R., 2020. Dobutamine stress testing in patients with Fontan circulation augmented by biomechanical modeling. PLoS One 15 (2), e0229015.

Sainte-Marie, J., Chapelle, D., Cimrman, R., Sorine, M., 2006. Modeling and estimation of the cardiac electromechanical activity. Comput. Struct. (ISSN: 00457949) 84 (28), 1743–1759. http://dx.doi.org/10.1016/j.compstruc.2006.05.003.

Sammut, E.C., Villa, A.D.M., Di Giovine, G., Dancy, L., Bosio, F., Gibbs, T., Jeyabraba, S., Schwenke, S., Williams, S.E., Marber, M., Alfakih, K., Ismail, T.F., Razavi, R., Chiribiri, A., 2018. Prognostic value of quantitative stress perfusion cardiac magnetic resonance. JACC: Cardiovasc. Imaging 11 (5), 686–694. http://dx.doi.org/10.1016/j.jcmg.2017.07.022.

Spaan, J.A., 1985. Coronary diastolic pressure-flow relation and zero flow pressure explained on the basis of intramyocardial compliance. Circ. Res. 56 (3), 293–309.

Truesdell, C., 1962. Mechanical basis of diffusion. J. Chem. Phys. 37 (10), 2336–2344.

Westerhof, N., Boer, C., Lamberts, R.R., Sipkema, P., 2006. Cross-talk between cardiac muscle and coronary vasculature. Physiol. Rev. 86 (4), 1263–1308.